Modeling the Performance and Failure of Elastomeric Coatings Under Erosive Cavitating Flows

by

Xiao Liao

A Dissertation Presented in Partial Fulfillment
of the Requirements for the Degree
Doctor of Philosophy

Approved August 2016 by the
Graduate Supervisory Committee:

Jay Oswald, Chair
Yongming Liu
Hanqing Jiang
Subramaniam Rajan
Rodrigo Platte

ARIZONA STATE UNIVERSITY

December 2016

ABSTRACT

Finite element simulations modeling the hydrodynamic impact loads subjected to an elastomeric coating were performed to develop an understanding of the performance and failure mechanisms of protective coatings for cavitating environments. In this work, two major accomplishments were achieved: 1) scaling laws were developed from hydrodynamic principles and numerical simulations to allow conversion of measured distributions of pressure peaks in a cavitating flow to distributions of microscopic impact loadings modeling individual bubble collapse events, and 2) a finite strain, thermo-mechanical material model for polyurea based elastomers was developed using a logarithmic rate formulation and implemented into an explicit finite element code.

Combining the distribution of microscopic impact loads and finite element modeling, a semi-quantitative predictive framework is created to calculate the energy dissipation within the coating which can further the understanding of temperature induced coating failures. The influence of coating thickness and elastomer rheology on the dissipation of impact energies experienced in cavitating flows has also been explored.

The logarithmic formulation has many desired features for the polyurea constitutive model, such as objectivity, integrability, and additive decomposition compatibility. A review and discussion on the kinematics in large deformation, including a comparison between Lagrangian and Eulerian descriptions, are presented to explain the issues in building rate-dependent constitutive models in finite strains. When comparing the logarithmic rate with other conventional rates in test examples, the logarithmic rate shows a better conservation of objectivity and integrability.

The modeling framework was validated by comparing predictions against temperatures measured within coatings subjected to a cavitating jet. Both the experiments

and models show that the temperatures generated, even under mild flow conditions, raise the coating temperature by a significant amount, suggesting that the failure of these coatings under more aggressive flows is thermally induced. The models show that thin polyurea coatings synthesized with shorter molecular weight soft segments dissipate significantly less energy per impact and conduct heat more efficiently. This work represents an important step toward understanding thermally induced failure in elastomers subjected to cavitating flows, which provides a foundation for design and optimization of coatings with enhanced erosion resistance.

ACKNOWLEDGMENTS

I would like to sincerely thank my advisor, Dr. Jay Oswald, who introduced me to computational mechanics and continually mentored me during the entire period of my studies and researches. He worked closely with me on this dissertation with his expertise, generous guidance, and endless ideas. I'm also very fortunate to be one of his first students and have the opportunity to participate in the early development of our lab code. These precious experiences helped me successfully start a career in the industry.

I would like to thank my committee members, Dr. Yongming Liu, Dr. Hanqing Jiang, Dr. Subramaniam Rajan, and Dr. Rodrigo Platte, from whose inspiring classes I gained solid fundamental knowledge to accomplish the project. The class notes and assignments had been very helpful for the research and will be a reference for my future work.

I would like to thank my labmates and close friends, especially Rui Yuan, Vipin Agrawal, Yiyang Li, Ilaksh Adlkha, Mehul Bhatia, Ruijin Cang, and Lei Liu, for the talks during the coffee time and hot pot time, for the nights we were working on assignments before deadline, and for the fun we have had in the last five years.

Last but not the least, I would like to thank my family: my parents and my great-grandmother for their support and encouragement. Thanks for letting me study overseas and always welcoming me back home. Special thanks to my beloved wife Jing Chen, who is always supportive, thoughtful, wise, and patient. I couldn't go through the hardest time without her support. It is such a wonderful thing to have her accompany in the long journey of life.

TABLE OF CONTENTS

CHAPTER Page

LIST OF TABLES

LIST OF FIGURES

Figure Page

Figure Page

Chapter 1

INTRODUCTION

Cavitation occurs when the vapor bubbles are created in a liquid due to a rapid decrease in pressure, e.g., as flows curve around high-speed naval components such as propeller blades, local changes in the fluid pressure can lead to explosive growth of bubble nuclei into cavities which then break up into individual vapor bubbles. As these vapor bubbles are swept into regions of higher pressures, the bubbles collapse violently, resulting in the creation of shock waves in the fluid, or when near a surface, an asymmetric collapse leads to the formation of a micro jet that impinges on the surface generating large pressures [1–6]. In a cavitating flow near naval components, the repetitive collapse of bubbles against the surface leads to erosive wear eventually causing component failure.

Recently, there has been an interest in developing polymeric coatings [7–9] to absorb and dissipate the intense hydrodynamic loads generated by cavitating flows through viscous deformation mechanisms. However, unlike metallic surfaces, where the relationship between material properties and erosion resistance have been extensively studied [10–15], the relationship between the material properties of polymers and their erosion resistance has not yet been clearly established. In particular, the effects of rheology and thermal stability are important factors in determining the cavitation erosion resistance of polymeric materials. Cavitation erosion tests conducted by Hattori and Itoh [16] demonstrated that the temperature rise of polymer specimens, including epoxy resin, polypropylene, and polyamide 66, subjected to cavitating flows was 10-20 times higher than for aluminum and stainless steel surfaces. As both the rheological and yield properties of polymers are highly sensitive to temperature, the

large amount of heating generated in polymeric coatings strongly suggests a thermal mode of failure.

Many studies have been conducted to estimate impact loads generated by bubble collapse and assess the resulting damage to the material surface. Tomita [17] performed an experimental study to analyze the impulsive pressures generated from single bubble collapses and demonstrated that small bubbles driven to collapse by a shock wave could generate large enough localized pressures to cause plastic deformation in materials. Okada [18] combined measurements of the area and depth of erosion pits with separately measured impact loads to estimate the impact energy which was correlated with the rate of volume loss in the material. Momma [19, 20] developed a new type of pressure transducer using a piezoelectric foil to detect cavitation pressure pulses, and attempted to correlate the pit size with the magnitudes of surface impact pressures. Franc et al. [21] measured surface impact loads in a high-speed cavitation loop by means of a flush-mounted pressure sensor and proposed that two-dimensional distributions of impacts should be used to characterize the aggressiveness of a cavitating flow that consider both the size of the impacted area and the load amplitude. As the micro jets are, in general, smaller than the transducers available to measure loads, characterization of peak surface pressures has been indirect, relying on inferences made from measurements of pit sizes, total impact forces, and plastic deformation. Veysset et al. [22] tested the responses of poly(urethane urea) (PUU) coatings to high-velocity microparticle impact and found that under microscopic loadings with high strain rate and high pressure, (PUU) presents a hyperelastic response instead of glassy-like brittle behaviour while no fracture or plastic indentation is observed after the impact. So it is not appropriate to adopt the above methods which rely on the damage measurement after the impacts to characterize the

cavitating loads. A more detailed review of investigations conducted to estimating cavitation loads is provided by Kim et al. [23].

Recently, polyurea has attracted an increasing interest in coating industry as an excellent candidate for protective coatings. It is widely reported that polyurea coatings can effectively improve the blast resistance of the substrate [24–26] and prevent ballistic penetration [27–29]. Moreover, the adhesive nature of polyurea makes it easy to apply on the substrate, usually just sprayed on, and provides the ability to retain the broken fragments generated when the structure is broken. So for cavitation erosion, these properties of polyurea make it a promising coating material on propellers or turbines. Additionally, polyurea coatings have other appealing features for naval applications such as waterproof, acids resistant, weather tolerant, and so on.

Hydrodynamic impacts during cavitation erosion of a surface are characterized by large local pressures (pressures greater than a gigapascal were inferred from measurements conducted by Momma and Lichtarowicz [19]) applied over very short time scales (on the order of microseconds [30]). Knowledge of the material response of elastomers, such as polyurea, is limited in such extreme loads, particularly for multiaxial stress states. Split-Hopkinson bar experiments have been conducted by several groups [31–34] to characterize the behaviors of polyurea at a strain rate of 10^3 s^{-1}. These experiments indicate that polyurea is sensitive to strain rate, i.e. there is a rubbery-to-glassy transition in the material response as the strain rate is increased. Pressure–shear plate impact experiments conducted by Jiao et al. [35–37] were able to probe the mechanical response of polyurea at pressures up to 9 GPa and shear strain rates of 10^6 s^{-1}. Youssef [38] studied the response of polyurea at strain rates of $10^7\,s^{-1}$ using laser-driven stress waves with nanosecond rise times, and verified that even at these extraordinarily high rates, the time-temperature superposition principle is valid for polyurea. A comprehensive treatment of the high strain rate effects in

elastomeric polymers, including polyurea, is discussed in the recent book edited by Barsoum [39].

From these and other experimental characterizations of polyurea, several constitutive laws, based on viscoelasticity, have been proposed for polyurea. El-Sayed [40, 41] proposed a viscoplastic model for large deformation by introducing plastic strain into the model to capture permanent material damage. Li [42] combined the hyperelastic and viscoelastic characteristics of polyurea into a new hyper-viscoelastic constitutive model. Shim [43] represented the long-term softening property by Gent elastic equations and the time-dependent response by nonlinear viscoelastic equations. Gamonpilas [44] developed a nonlinear viscoelastic constitutive model for polyurea by assuming a separable time and strain dependence. Amirkhizi et al. [45] proposed an experimentally based model including temperature, pressure, and strain rate dependence. Under the assumption of small deformation, this model decomposes the strain into a hyperelastic dilatancy part and viscoelastic deviatoric part. The temperature is computed from the dissipated energy which can be obtained from the creep strain. This model successfully reproduces results of various independent tests, including the pressure–shear plate impact experiments performed by Jiao and Clifton [35], and has been widely used in applications involving blast loads [46, 47].

One limitation of the Amirkhizi model is the lack of compatibility of large rotation deformation. To generalize this model, the decomposition expressions of the volumetric-deviatoric and elastic-creep strains need to be rewritten in large deformation kinematics. Moreover, since the strain rate is involved, the objectivity of the constitutive model must be considered.

The multiplicative decomposition rule, i.e. $\boldsymbol{F} = \boldsymbol{F}_e\boldsymbol{F}_p$ and $\overline{\boldsymbol{F}} = J^{-\frac{1}{3}}\boldsymbol{F}$, is widely used in finite deformation constitutive models. However, as discussed in [48–51], the non-uniqueness property of multiplicative decomposition leads to several issues

such as nonobjective elastic deformation, complicated separation of deformation rate and elastic relation invariance. The non-uniqueness issue of the multiplicative decomposition formula is reviewed by Naghdi in [52]. Furthermore, as pointed out by Bažant [53], when decomposing the volumetric-deviatoric strain, two unappealing consequences arise (except Hencky strain), the isochoric strain $\boldsymbol{\epsilon}_D$ tensor is not traceless ($\text{trace}(\boldsymbol{\epsilon}_D) \neq 0$) and is dependent from the volumetric stretch ($\boldsymbol{\epsilon}_D = f(\epsilon_V)$).

As shown in [53], derived from a multiplicative decomposition of deformation gradient, the Hencky strain can be written in an additive expression without the issues that other strains measures have and presents a consistency between two decomposition formulas. Xiao [54, 55] comprehensively investigated the relationship between logarithmic strain $\ln \mathbf{V}$ and stretching (or deformation rate) tensor $\mathbf{D}$ and concluded: 1) the stretching tensor is identical to the objective rate form of Hencky strain with a unique choice of spin tensor, which is named the logarithmic spin, and 2) the Hencky strain and Cauchy stress form a work-conjugate pair.

In a general standpoint, Xiao et al. [56, 57], examined the Hencky strain and logarithmic rate framework with the problems reported by early attempts to construct Eulerian constitutive frames like the integrability issue pointed out by Simo [58] that the integral of the objective stress rates, such as the Jaumann rate and Green-Naghdi rate, along a closed path will not be zero. It is shown that the logarithmic rate formula avoids introducing a fictitious intermediate configuration, e.g., the artificial state after pure plastic deformation $\mathbf{F}_p$, and keeps the additive strain separation consistent with the energy separation, e.g. the plastic strain ϵ_p is uniquely and fully associated with the irrecoverable energy.

As a result of these paragraphs, the logarithmic rate formulation has several attractive features. First, the strain rate variable in the small-strain formulation can be directly replaced by the deformation rate tensor without any modification to the

elastic tangent moduli (see section 10.3 in [57]). Second, the additive decomposition is automatically inherited for both volumetric-deviatoric and viscoelastic-plastic deformation rate separation. Third, the objectivity requirement of the rate form is fulfilled. Finally, the logarithmic rate shows evidence of integrability.

Under the logarithmic rate form formulation framework, a nonlinear constitutive model for polyurea is introduced. The molecular statistic based Arruda-Boyce hyperelastic model [59] is used to describe the stretch-dependent stress response. Moreover, a plastic model is adopted to represent the stress softening behavior, i.e. the loss in stiffness or plastic residual strain left by prior loads.

To summarize, we use the viscoelastic model developed by Amirkhizi et al. extended to a co-rotational, large deformation kinematic description, to analyze the energy dissipated from hydrodynamic loads representing those generated by the collapse of vapor bubbles near a coated surface. While this model does not account for damage or strain–dependence of the dynamic moduli, it gives a reasonable description of the dynamic behavior of polyurea, accurately accounts for the effects of pressure and temperature on viscous flow, and provides a thermodynamically consistent rate of energy dissipation. While a more sophisticated model, featuring damage evolution and strain dependent moduli would, in principle, provide a better description, parameterization of such a model requires material characterization in conditions that are extremely difficult to reproduce in controlled experiments. Thus, limited by incomplete knowledge of the precise nature of the surface loadings generated under cavitating flows and the material response under extreme pressure and strain rates, the objective of this study is to provide a framework for semi–quantitative analysis that can be used to generate new insights to the failure mechanisms of elastomeric coatings subjected to cavitating flows.

Chapter 2

A STATISTICAL MODEL OF CAVITATION AGGRESSIVENESS

In this chapter, a brief introduction to the nucleation, growth, and collapse of the cavitation bubbles will be presented. The bubbles collapse leads to a high pressure and short duration local impulsive load on the solid material surface. The massive number of the bubbles magnifies the damage resulted from the impacts and eventually leads to a macroscopic failure. Thanks to well-developed laboratory cavitation erosion testing techniques, the bubble collapse loads can be measured in amplitude and duration and a correlation between the experimental observation and FEA input parameters can be established.

2.1 Introduction to Bubble Impact

Cavities, or bubbles, are nucleated in liquids under sudden pressure drop. A bubble nuclei, referring to a microbubble existing in liquid flow around solid objects, travels with a velocity V_f determined by the dynamic flow. Once the local pressure reduces, the nuclei rapidly grows into various sizes from microns to millimeters. A well known dimensionless number, called the cavitation number, expresses the relationship between the pressure and the velocity:

$$\sigma = \frac{2\left(p - p_v\right)}{\rho V_f^2} \tag{2.1}$$

where p is the local pressure and p_v is the vapor pressure of the fluid. The cavitation number is an effective measurement of the extent of cavitation development in a flow. The smaller the value is, the liquid is more likely to form cavities because according

to the Bernoulli principle, a larger flow speed leads to a lower pressure that is more close to the vaporize point.

The bubble collapse is triggered when the local pressure increases to a critical point $p = p_c$. This critical pressure is related to many factors including the surface tension, vapor pressure, and bubble radius ([60]). According to Rayleigh's model of bubble dynamics, the duration of the bubble collapse, which is also called the Rayleigh time, is related to the collapse pressure, which will be shown in the following section.

If the bubble collapses close to a solid wall, a re-entrant jet is formed and impacts the solid wall with high speed. A highly concentrated and dynamic impulsive pressure is then induced on the solid surface which can cause severe local deformation on the material. In an energy point of view, the potential energy of the bubble is all converted into kinetic energy when it collapses. A portion of the kinetic energy is carried by the re-entrant jet and converted into external work done to the material during the impact. An illustration of the bubble collapsing process is shown in Fig. 2.1

The velocity of the re-entrant jet depends on the bubble collapse pressure p_c. In order to quantify the relation between V_{jet} and p_c, Chahine et al. [63] conducted CFD simulations of the bubble evolution [64–66] and established a relationship between the collapse pressure and jet speed. In their bubble dynamics simulations, bubbles were grown to a 2 mm radius with their centers 1.5 mm away from a rigid wall. At the same time, the pressure was raised to the collapse pressure, ranging from 100 kPa to 15 MPa. Then the resulting velocities of the water jets vary due to the different driving pressures. A linear fit is presented between the square root of the collapse pressure and re-entrant jet velocity, shown in Fig. 2.2

$$V_{jet} = 4.6\sqrt{p_c/\rho} \tag{2.2}$$

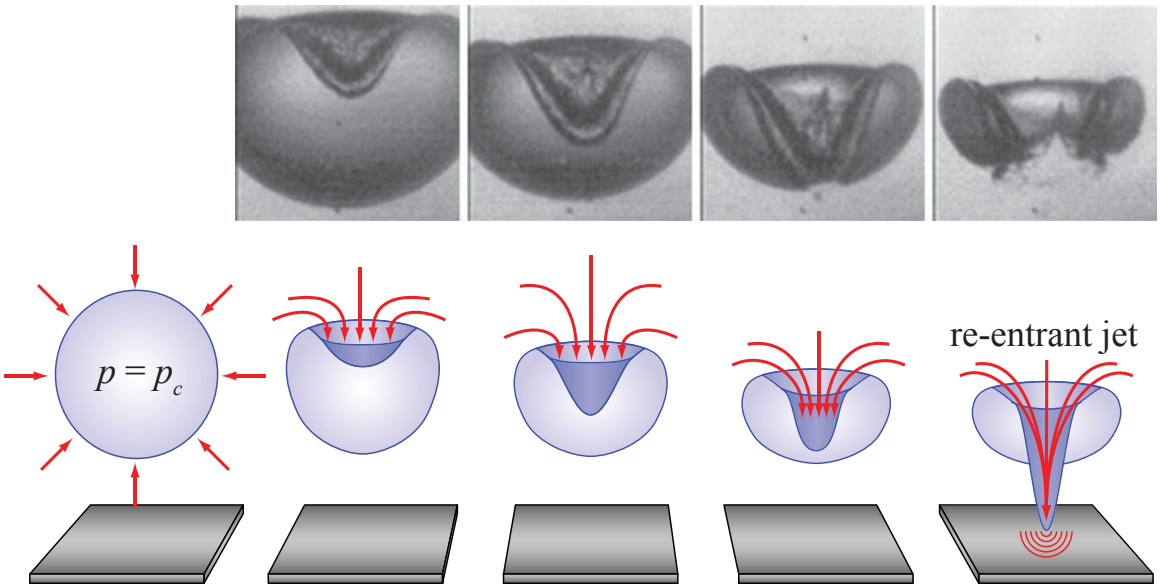

Figure 2.1: The process of a bubble collapsing and the formation a re-entrant water jet recorded by Chahine et al. [61, 62].

where ρ is the density of water. This equation also agrees to the previous studies by Blake [6].

From the conservation of momentum relations, the pressure of re-entrant jet when it arrives the wall is obtained:

$$p_{jet} = \rho c V_{jet} \tag{2.3}$$

where c is the sound speed of water. The p_{jet} denotes the pressure at the tip of the re-entrant water jet when exerted on a flat rigid surface. Fig. 2.3 shows the dynamic interaction between the re-entrant water jet and surface material. The re-entrant jet has a curved surface around the jet tip, due to the collapsing intensity difference within the bubble: the center of the bubble generates the highest jet speed which develops into the jet tip. So a factor of 0.6, which is fitted from bubble dynamics simulation results as shown in Fig. 2.4, is multiplied to the tip velocity as an estimation of the average velocity of the whole re-entrant jet. Then the maximum pressure applied

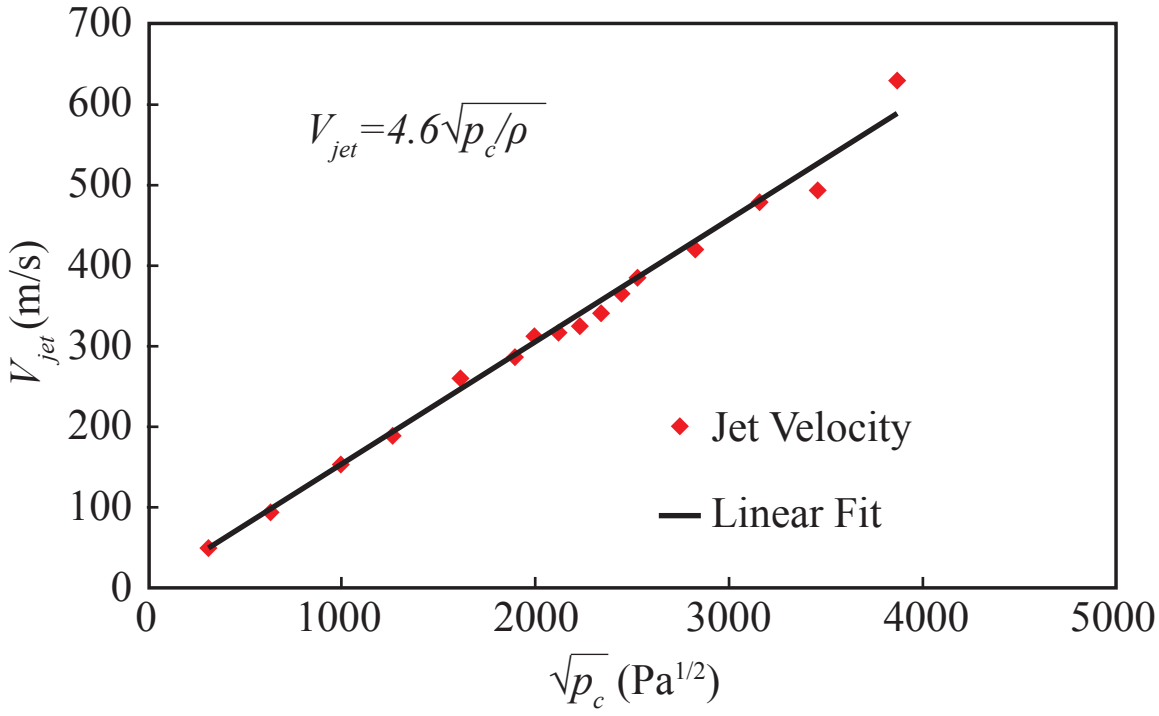

Figure 2.2: Relation between the re-entrant jet velocity and the pressure driving the bubble collapse (reproduced from Fig. 6.9 in [67] with permission from Dynaflow).

on the solid material is estimated according to the force equilibrium equation for impacts:

$$\begin{aligned} p_m &= 0.6\frac{\rho_s c_s}{\rho_s c_s + \rho c}\rho c V_{jet} \\ &= 0.6\gamma\rho c V_{jet} \end{aligned} \tag{2.4}$$

where ρ_s and c_s are the density and sound speed for the solid surface material. The parameter γ is related to the difference in impedance between the fluid and the surface material and approaches unity in the limit of a perfectly rigid surface. However, since the impedance of polyurea is comparable to that of water, it is not appropriate to ignore this factor. In fact, γ is around 0.6 for polyurea when the impact initiates and makes a significant difference to the impulsive pressure.

Although a single bubble collapse brings little energy into the material and would

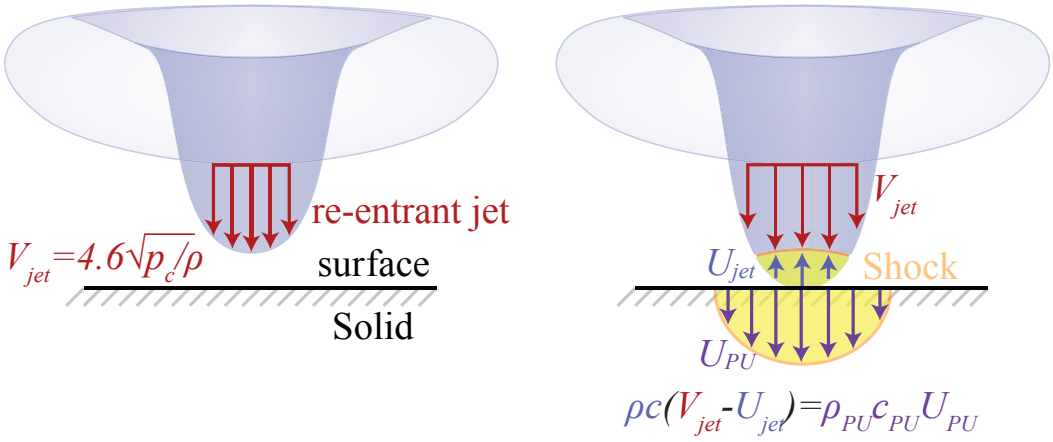

Figure 2.3: Generation of shock wave from water jet impact on solid surface.

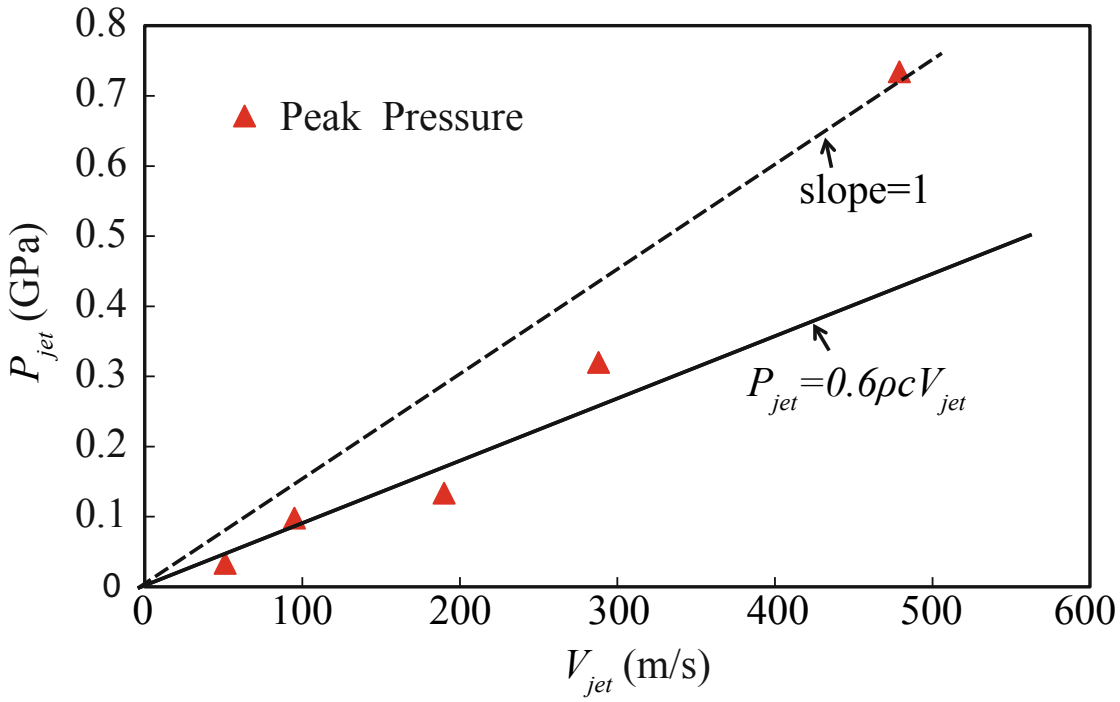

Figure 2.4: Relation between peak impact pressure and the jet velocity (reproduced from Fig. 6.10 in [67] with permission from the author).

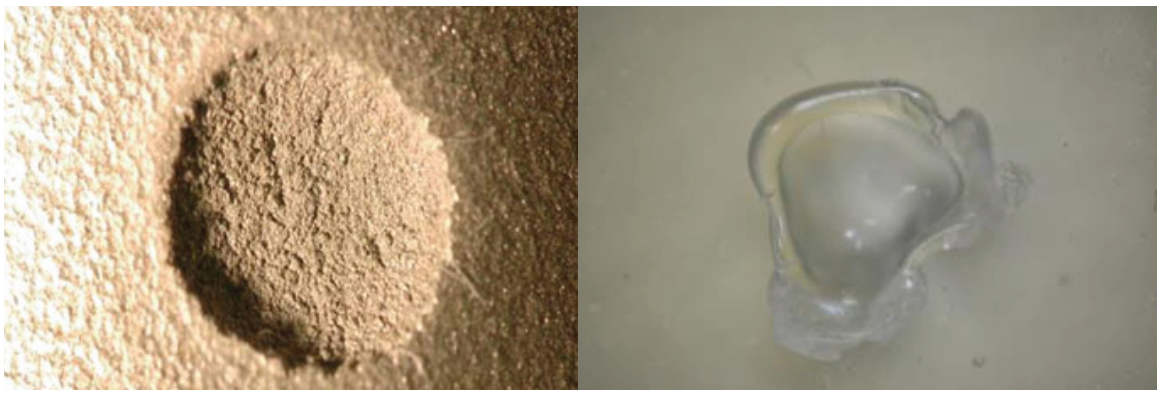

(a) (b)

Figure 2.5: Typical cavitation erosion pattern induced by cavitation erosion on (a) metal and (b) polyurea surfaces [68].

not cause visible damage, the material damage accumulates under the repetitive impact forces produced by a cavitating flow. Macroscopic failure of the material occurs when the cavitation damage increases over the failure criterion. As shown in Fig. 2.5, the pattern of the cavitation induced pit on metal is different from that on polyurea. The pit on metal has a clear edge while the pit on polyurea shows a swelled edge and melt geometry. The damage criterion can be represented in many forms depending on the material, e.g. the temperature rise or pressure, which are critical factors affecting the properties of polymers. In this work, the dissipated energy is regarded as the damage of the material as it is converted into heat and not recoverable. So to understand the macroscopic failure, the premise is to have a robust model which is able to precisely model the impact on the material induced by single bubble collapse and predict the increment of the dissipated energy within the material. Then the overall damage within a period and area can be predicted by integrating the dissipated energy over all the impacts.

Since bubble collapse occurs over a time span measured in microseconds, high-speed cameras and advanced imaging technologies are applied to capture its shape

change. By using materials with a low yielding criterion, e.g. indium [17], the dimension and intensity of the bubble collapse load can be estimated by measuring the radius and depth of the pit left on the solid surface. Numerical models are also created to predict bubble collapse characteristics including collapse pressure, maximum radius and re-entrant jet velocity and radius. Based on the Rayleigh-Plesset model, the relations between bubble parameters and their effects on the resulting impulsive pressure are well understood.

Although the dynamic behavior of a single bubble can be directly observed in laboratory and simulated with robust models, it is challenging to correlate the single bubble to the characteristics of a cloud of bubbles in a real cavitation environment. Several experiments have been developed to produce a controlled cavitation environment, such as vibratory cavitation apparatus [69], cavitating jets [19, 70, 71] and high-speed cavitation tunnels [72]. But a few numerical models exist to characterize the multiple bubbles. As the large quantity and the diversity of bubbles require a heavy computational resource, statistical approximations such as sampling and regression modeling are usually used to simplify the problem.

Another challenge is to relate the cavitation fluid aggressiveness to the material damage. The pits induced by the cavitating impacts on metallic surfaces can be analyzed in terms of width and depth to deduce the pattern of the incoming loads. But the pits are built by the cumulative bubble collapse loads with different parameters. Philipp and Lauterborn [73] showed that a single bubble collapse can cause more than one pit. Moreover, Dular et al. [74] showed that a single pit can be caused by more than one bubble collapse. So it is extremely complex to precisely characterize the formation process of pits from cavitation bubbles and retrieve the characteristics of the bubble collapse impacts from the corresponding pit. Also, as a ductile material, polymers usually do not form pits under cavitation environment.

The goal of this chapter is to establish a statistical model to convert laboratory cavitation environment measurements to bubble collapse load parameters. Instead of analyzing the dimensions of the pits, we related the spatial span of bubble collapse loads to the duration of the load using the Rayleigh time as a bridge. A correlation between the macro-scale cavitation flow parameters and the micro-scale bubble collapse load parameters is finally built to convert the material heating under single bubble impact predicted by FEM to the overall material erosion under cavitating jet environment.

2.2 Cavitation Impulsive Loads

The surface pressures on a plate induced by the bubble collapses under a cavitating jet were measured by our co-workers from Dynaflow. They provided us the peak and duration of all the pressure signals and we built the numerical model based on the bubble collapse distributions. In order to better explain our model, we briefly summarize their experimental method here. The pressures were recorded in the Dynaflow laboratory using a high-frequency response pressure transducer to characterize the impulsive pressure load distribution at two jet velocities, one with the dynamic pressure at the exit of the jet nozzle, denoted as p_{jet}, equals to 2.75 MPa and the other with 5.52 MPa. So according to the equation $p_{jet} = \frac{1}{2}\rho v^2$, the cavitating jet velocity at the nozzle is 50 m/s for $p_{jet} = 2.75$ MPa and 100 m/s for $p_{jet} = 5.52$ MPa. This velocity of the cavitating jet will be significantly dissipated when arriving the solid surface, but the actual velocity of the cavitating jet at the solid surface is irrelevant. We will just use the jet pressure p_{jet} instead of the jet velocity as the measure of cavitation environment intensity to avoid confusion with the re-entrant jet velocity V_{jet}. The measurement facility and methodology for analyzing the pressure signals are described in detail by Singh et al. [30], so only a brief summary of the

impulsive pressure load measurement is given here. The pressure transducer (PBC model 102A03) has a response time of 1 μs and a resonant frequency of 500 kHz. A Plexiglas (PMMA) insert was used both to protect the tip of the transducer and reduce the effective sensing area from 19.63 mm^2 to 3.14 mm^2. Pressure signals from a 2.19 mm diameter cavitating jet were sampled for different jet pressures with the transducer placed at a standoff of 25.4 mm from the jet nozzle. The measured signals were analyzed to extract the peak amplitudes and peak widths of all detected pulses over a 60 second recorded sample. Pressure peaks are detected between two pairs of crossings of a threshold pressure value of 65 kPa.

As the signals are usually noisy, a threshold amplitude is used to filter the irrelevant small peaks. Chahine et al. [75] validated that the threshold processing method does not significantly affect the statistic characteristics of the impact signals. They compared the signal width and height distributions processed by different amplitude thresholds with original data and found that the difference is minimal and the overall trend stays the same. The pulse width is measured as the time between the points where the pressure reaches 50% of the peak pressure amplitude. From the measured collapses, a two-dimensional impact distribution is generated, relating the density of collapse events in terms of their peak pressures and peak durations.

Fig. 2.7 illustrates a representative bubble collapse over the surface of the transducer. The collapsing bubble generates a water jet of radius R_{jet} which impacts the surface, generating a microscopic surface load over a characteristic hydrodynamic loading radius R_h with a local pressure amplitude of p_m. While the duration τ of this bubble collapse load can be directly recorded, the hydrodynamic loading radius is 2-3 orders of magnitude smaller than the size of the sensitive area of the pressure transducer, and so the recorded measurement does not provide an accurate characterization of the microscopic impulsive pressures exerted on the material surface.

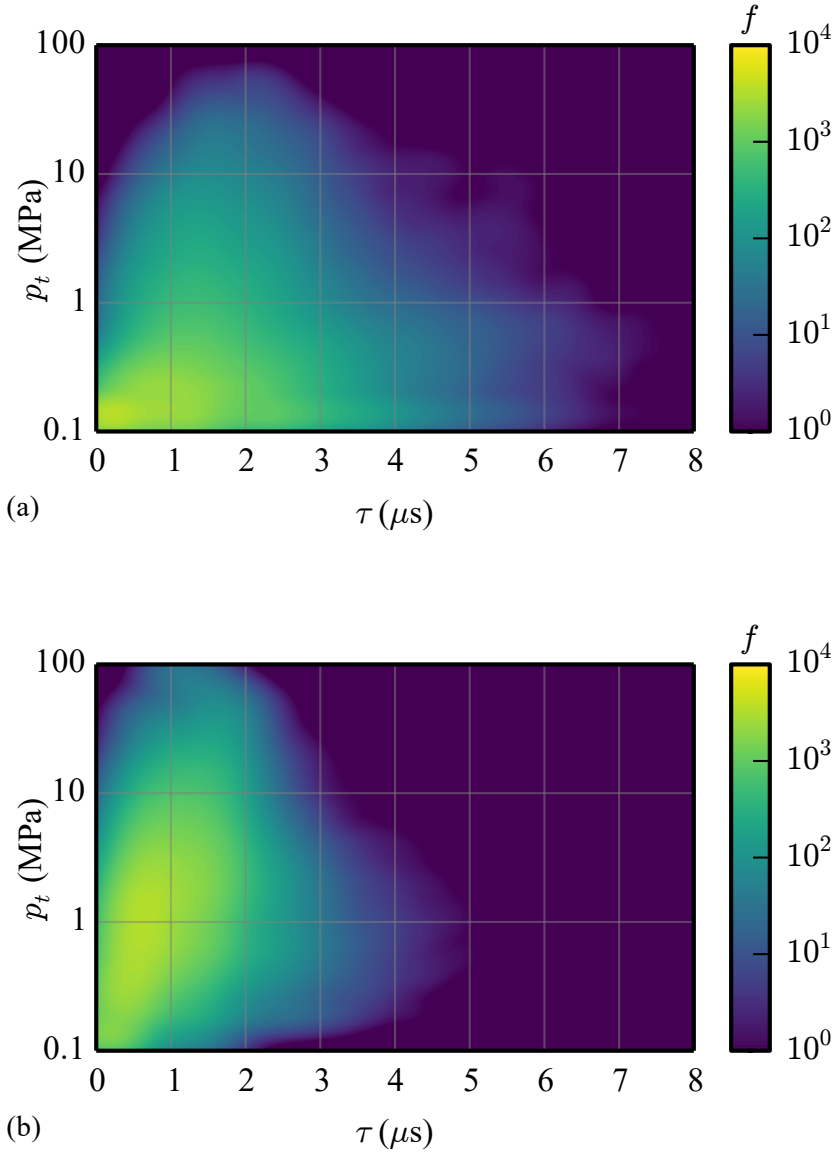

Figure 2.6: Frequency density of pressure peaks as a function of peak amplitude and peak duration for jet pressures of (a) 2.75 MPa and (b) 5.52 MPa. The units of the frequency density are $\frac{1}{\mathrm{s}} \cdot \frac{1}{\mu\mathrm{s} \cdot \log(\mathrm{MPa})}$.

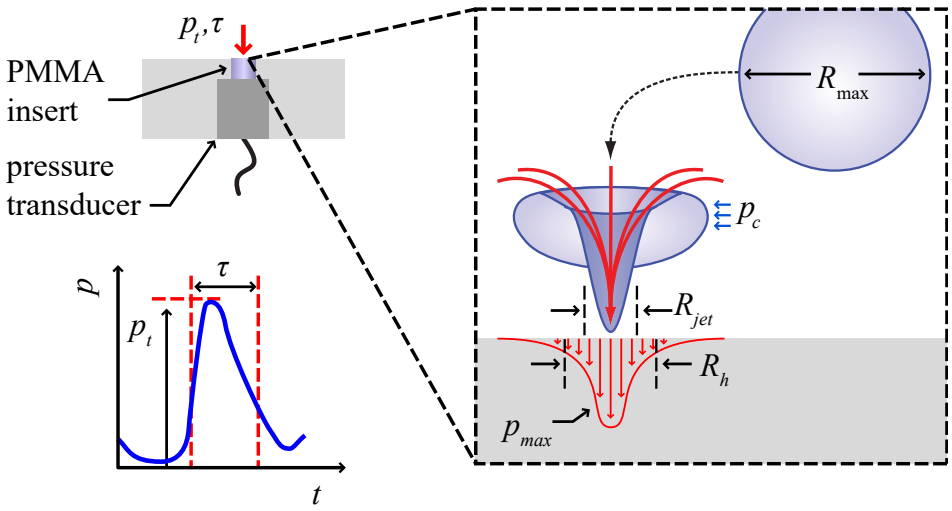

Figure 2.7: Measurement of impact load from a jet resulting from the collapse of a bubble of initial radius $R_{\max}$..

Instead, the average pressure p_t, i.e., the total force generated by the microscopic surface pressure distribution divided by the sensitive area of the pressure transducer, is recorded.

The distributions of measured impacts under 2.75 MPa and 5.52 MPa jets is shown in Fig. 2.6. Comparing the density distribution contours under two cavitating jet pressure, the higher pressure lifts the contour peaks up in p_t axis while narrowing the range in τ axis, indicating that a more intensive cavitating jet produces more powerful bubble impacts. The integrals of the density distribution contours are the average numbers of impacts recorded per second during the experiment:

$$N_{total} = \int_{-\infty}^{\infty}\int_{0}^{\infty} f(\tau, \log[p_t])d\tau d\log[p_t] \tag{2.5}$$

The numbers are 6000 s^{-1} and 4800 s^{-1} for 5.52 MPa and 2.75 MPa jet pressures, respectively.

In order to model the dissipation of energy from individual impact events, it is necessary to translate the distribution of pressure pulses from the macroscopic pa-

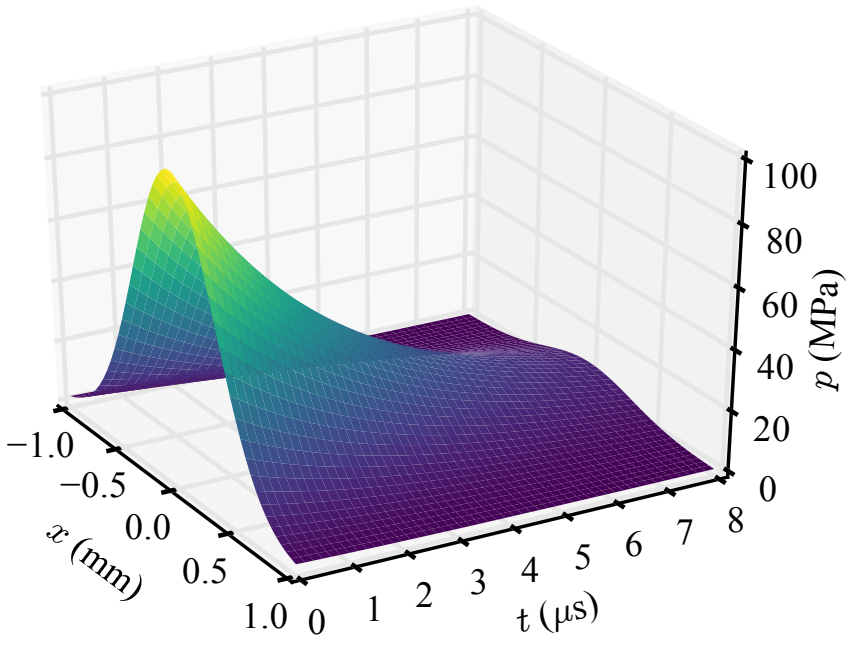

Figure 2.8: Example bubble collapse load in 3D space of radius and time with typical characteristic parameters: R_h =0.5 mm, τ =3.41 μs, p_m =100 MPa.

rameters, p_t and τ, to microscopic parameters, R_h and p_m. Two linearly independent constraints are needed to map between the macroscopic and microscopic distributions. Each impulsive surface load is modeled by a *representative* microscopic load distribution which assumes a Gaussian distribution of pressure in space and an exponential decay of pressure in time. The microscopic load distribution is expressed as

$$p(r,t) = p_m e^{-t/\tau} e^{-(r/R_h)^2}, \tag{2.6}$$

where p_m is the maximum pressure exerted on the surface at the local microscopic scale. Fig. 2.8 shows the shape of the load in time and space. Given the representative load distribution, the total force generated by the microscopic load distribution is

equated to the total force measured by the pressure transducer:

$$p_t A_t = \int_0^{2\pi} \int_0^{\infty} p_m e^{-(r/R_h)^2} dr d\theta = \pi p_m R_h^2, \tag{2.7}$$

where $A_t = 3.14$ mm^2 is the sensing area of transducer.

The second constraint arises from the relationship between the maximum size of a bubble and its characteristic time scale. According to the Rayleigh model [1], the characteristic time of a bubble collapse is determined by the maximum bubble radius $R_{\max}$, the driving collapse pressure p_c, and the fluid density ρ:

$$t_R = R_{\max} \sqrt{\rho / p_c}. \tag{2.8}$$

Based on the numerical simulations reported by Chahine et al. [67], the duration of the hydrodynamic loading at the surface is proportional to the Rayleigh time over a wide range of bubble sizes and standoff distances. Thus we approximate the duration of the hydrodynamic load as $\tau = \alpha t_R$, with a parameter α:

$$\tau = \alpha t_R \tag{2.9}$$

where the factor α is determined by the normalized standoff between the bubble center and the wall X/R_{max}. As shown in Fig. 2.9, the temporal shapes of the shock loads with the same normalized standoffs are very similar. Besides, as the bubble center moves away from the wall, the resulting shock load on the surface will have a smaller amplitude and shorter duration, because the re-entrant jet needs to travel a longer distance to reach the wall and this will cause a larger loss in the impact momentum. By fitting an exponential function following the shock decay term in Eq. (2.6), the value of α can be estimated for different standoffs, e.g., $\alpha = 0.05$ for $X/R_{max} = 1.05$ and $\alpha = 0.025$ for $X/R_{max} = 1.25$. In a real cavitation environment, bubbles collapse at a range of different standoffs which is not possible to measure with

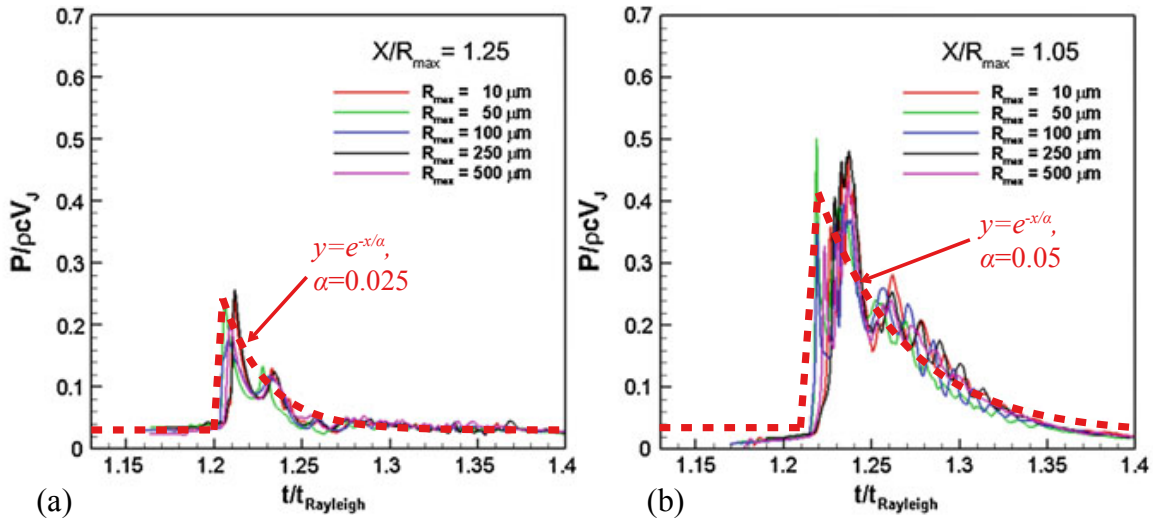

Figure 2.9: Bubble collapse load history from CFD simulations with normalized standoff distance (a) 1.25 and (b) 1.05 fitted with exponential function (using Fig. 6.17 in [67] with permission.

current experimental capabilities. According to [63], if the standoff is too small, e.g. $X/R < 0.75$, the re-entrant jet directly hits the wall before it is fully developed and accelerated to a large velocity. Also, if the standoff is too large, e.g. $X/R > 1.25$, the re-entrant jet will lose its speed and pressure as it travels to the wall. We therefore take $X/R_{max} = 1.25$ as an effective bubble collapse standoff with a corresponding value of $\alpha = 0.025$.

Combining Eqs. (2.2) and 2.7, the maximum pressure applied on the surface is calculated as:

$$p_m \approx 2.76\gamma c\sqrt{\rho p_c}, \tag{2.10}$$

where c is the fluid sound speed.

As reported by Chahine et al. [76], the hydrodynamic loading radius is proportional to the maximum bubble radius:

$$R_h = \beta R_{\max} \tag{2.11}$$

where the constant of proportionality, $\beta = 0.15$. This scaling factor β is also sensitive to the standoff distance and significantly affects the energy dissipation within the material. A discussion of the relation between scaling factor and energy will be presented in section 4.2.

Combining Eqs. (2.8) and (2.10), the maximum bubble radius $R_{\max}$ is related to the temporal parameter τ by:

$$\beta\tau p_m \approx 2.76\alpha\gamma R_h c\rho. \tag{2.12}$$

Solving Eqs. (2.7) and (2.12) for R_h and p_m gives:

$$\begin{aligned} R_h &= \left(\frac{\beta A_t p_t \tau}{2.76\alpha\gamma\pi\rho c}\right)^{1/3} \\ p_m &= \left(\frac{\left(2.76\alpha\gamma\rho c\right)^2 A_t p_t}{\pi\left(\beta\tau\right)^2}\right)^{1/3} \end{aligned} \tag{2.13}$$

From each recorded pressure peak, the macroscopic parameters, p_t and τ are translated into the microscopic variables p_m and R_h using Eq. (2.13). From this data, we construct an impact density distribution as a function of the hydrodynamic loading radii and maximum surface pressures. The resulting distribution is shown in Fig. 2.10.

A uniform grid of sampling points is built upon the probability distribution contour to simulate in the FEM model. Each sampling point with impulsive pressure radius and amplitude is taken as an input loading in the FEM model and the resulting coating behavior is the output. The choice of samples is based on the total energy E_{total} [1] carried by the bubbles which can be calculated as:

$$E_{total} = \frac{4}{3}\pi p_c R_{max}^3 \tag{2.14}$$

In total 71 sampling points are selected and marked with crosses in Fig. 2.10. If summing up the total energy from sampling points multiplied by the frequency of

represented signals, the resulted value should be approximately equal to the cumulative total energy per second:

$$\sum_{i} E^{i}_{total} \approx \sum_{j=0}^{N_{sample}} E^{j}_{total} N^{j} \tag{2.15}$$

where the index i denotes the i^{th} bubble collapse signal recorded in the experiment and j denotes the j^{th} sampling point in Fig. 2.10 while E^{i}_{total} and E^{j}_{total} are the corresponding bubble total energies. N^{j} is the frequency of the j^{th} sample.

We also investigated the load frequency distributions along load radius and maximum pressure under different jet pressures. As shown in Fig. 2.11, the majority of the bubbles generate a load with the radius less than 0.2 mm and peak pressure below 200 MPa. Thus, most of the bubbles in the cavitating bubble cloud are with the radius $R_{\max}$ around 1.0 mm. The jet driven by a higher pressure (5.52 MPa) generates larger load radius (0.15 mm) and larger peak pressure (100 MPa) than the jet driven by lower pressure (2.75 MPa).

To summarize, the path we took to describe the cavitating fluid aggressiveness is to relate the experimental measurement to the microscopic hydrodynamic pressure load parameters. By converting the distribution of the pressure signals from experiment to the distribution of bubble collapse impact loads, the cavitation intensity including load peaks, load durations, and load sizes, is successfully represented by the Gaussian pressure function. Compared with the method that indirectly correlates the parameters of cavitation pits to the loads, our approach directly obtains the load parameters from transducer records during the experiment based on bubble dynamics and CFD simulations. Moreover, different from metal surfaces, polyurea coatings do not generate microscopic pits under cavitation environment, thus it is also essential to construct this new method to characterize the fluid aggressiveness.

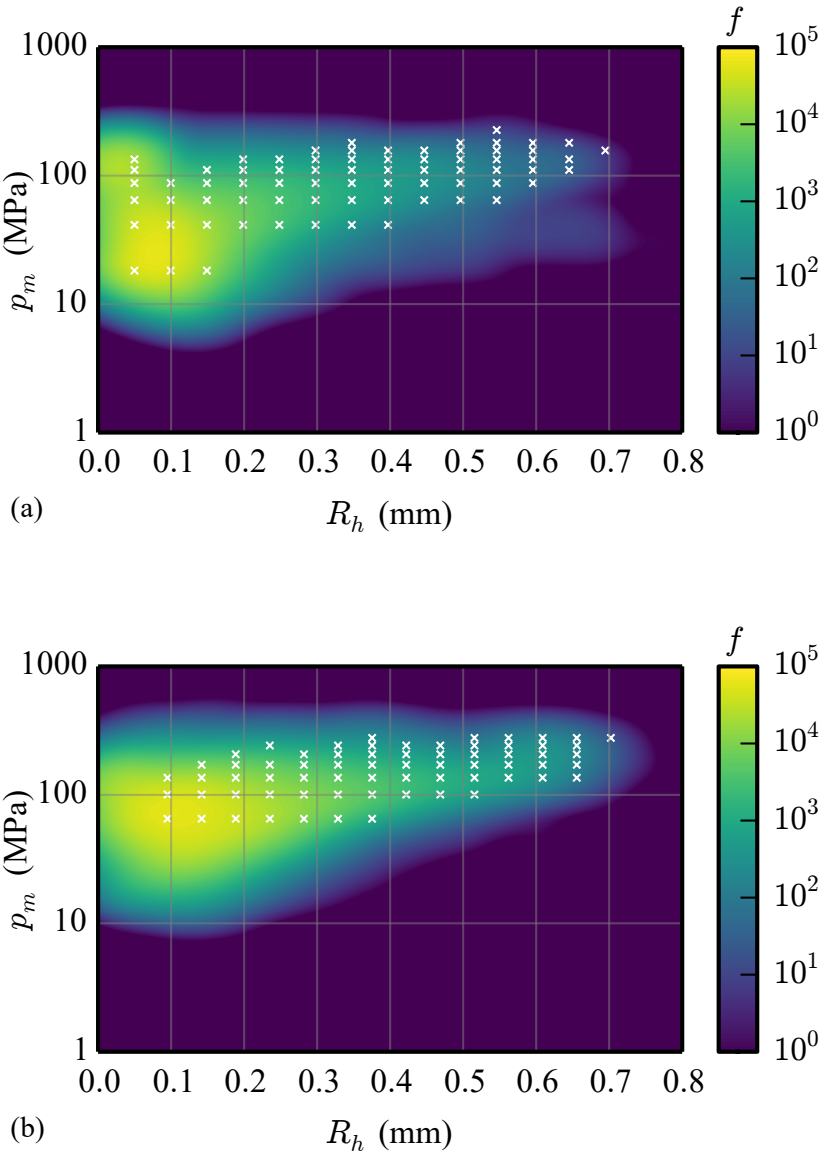

Figure 2.10: Frequency density distribution of impacts as a function of peak surface pressure and characteristic bubble size at a (a) 2.75 MPa and (b) 5.52 MPa jet pressure. Sampling points for calculating energy dissipation are marked by white cross symbols. The units of the frequency density are $\frac{1}{\mathrm{s}} \cdot \frac{1}{\mathrm{mm} \cdot \log(\mathrm{MPa})}$.

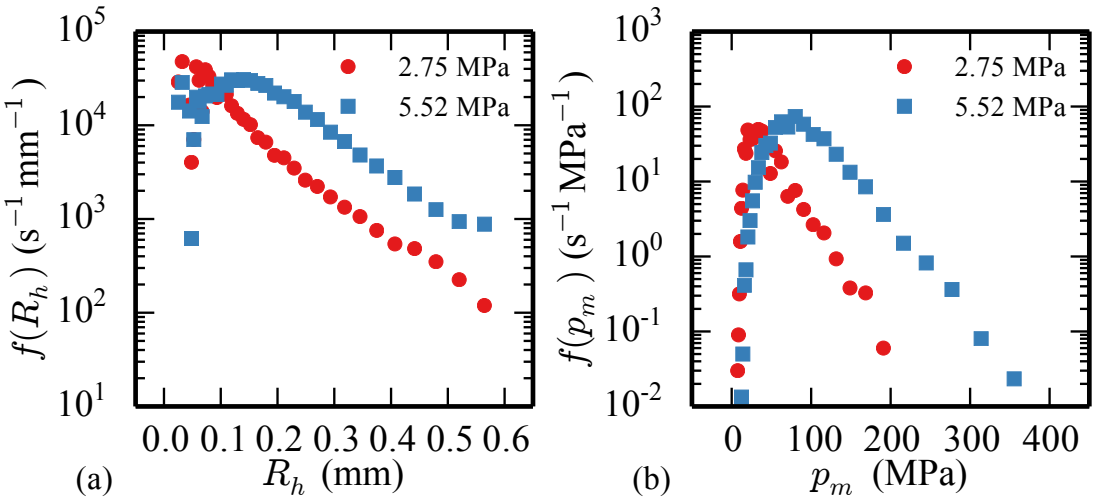

Figure 2.11: Frequency density of loads with different radiis and maximum pressures.

Chapter 3

MATERIAL MODEL FOR POLYUREA

The constitutive model used for polyurea is based on an additive decomposition of deviatoric stress and pressure

$$\boldsymbol{\sigma} = \boldsymbol{\sigma}' - p\boldsymbol{I}. \tag{3.1}$$

since elastomers respond very differently to hydrostatic and deviatoric loadings: the bulk response is usually elastic and stiff while the shear response involves a viscoelastic relaxation mechanism that arises time dependence. Accordingly, the additive relation also exists in strains:

$$\boldsymbol{\epsilon} = \boldsymbol{\epsilon}' + \epsilon_h \boldsymbol{I} \tag{3.2}$$

where $\boldsymbol{\epsilon}'$ is the deviatoric strain and ϵ_h volumetric strain.

The bulk response of the polyurea is represented by the Lennard-Jones model introduced in section 3.2.1. The shear response is modeled as a viscoelastic solid, and the effects of temperature and pressure on the relaxation spectrum are incorporated using the model of Amirkhizi et al. [45]. Compared with other viscoelastic material models, this model provides a reliable description of the thermal dynamic behavior of polyurea and a sound prediction of energy dissipating rate $W_D(r, y)$, which can be regarded as a measure of the damage. It also considers the various factors affecting the mechanical properties of polyurea such as pressure effects, stiffness retardation, and strain rate dependence.

According to viscoelasticity theory, the deviatoric stress at time t in finite strain with small rotation can be directly generalized from classical linear viscoelasticity

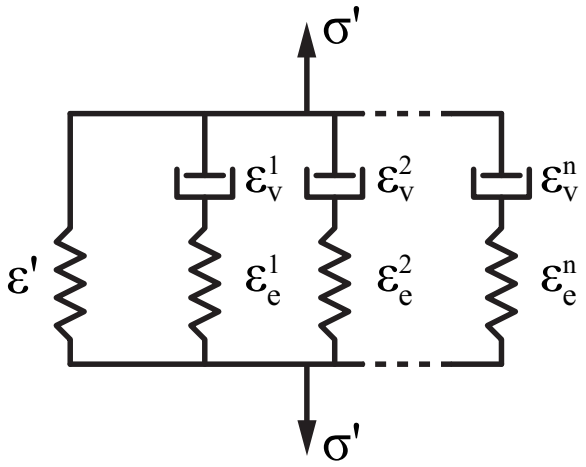

Figure 3.1: Schematic of a Maxwell-Wiechert model.

equation

$$\boldsymbol{\sigma}' = \int_{-\infty}^{t} G(t-\tau)\dot{\boldsymbol{\epsilon}}'(\tau)d\tau \tag{3.3}$$

where $G(t-\tau)$ is the relaxation function which represents the time dependence of the material shear stiffness. The strain rate $\dot{\boldsymbol{\epsilon}}'(\tau)$ can be replaced by the deviatoric deformation rate $\boldsymbol{D}'(\tau)$ under the small deformation assumption. To separate the elastic strain and creep strain, i.e. the strains associated with the recoverable energy and irrecoverable energy respectively, the additive decomposition is applied again as

$$\boldsymbol{\epsilon}' = \boldsymbol{\epsilon}_e + \boldsymbol{\epsilon}_v, \tag{3.4}$$

where $\boldsymbol{\epsilon}_e$ is the elastic strain and $\boldsymbol{\epsilon}_v$ is the creep strain.

For large deformations, Eq. (3.3) is no longer valid because

$$\boldsymbol{D}'(\tau) \neq \dot{\boldsymbol{\epsilon}}'(\tau), \tag{3.5}$$

and so the strain measurement must be described from either the Lagrangian or Eulerian configuration. The deformation rate tensor $\boldsymbol{D}$ is defined as the symmetric part of velocity gradient $\boldsymbol{L}$ and therefore is not the derivative of strain.

3.1 Kinematics

3.1.1 Lagrangian Description

To generalize the material model for finite deformations, one of the common paths is to use stress/strain variables in the reference configuration. One of the energy conjugate pairs of the Lagrangian variables is the deformation gradient $\boldsymbol{F}$ and the first Piola-Kirchhoff stress $\boldsymbol{P}$. The energy equation is

$$\dot{w} = J^{-1}\boldsymbol{P} : \dot{\boldsymbol{F}} \tag{3.6}$$

where $\dot{w}$ is the energy rate per volume. Then instead of an additive decomposition, a multiplicative decomposition is required to distinguish the deformations associated with different forms of energies. For polyurea, the volumetric-deviatoric decomposition is needed due to its distinct bulk and shear behaviors:

$$\boldsymbol{F} = J^{\frac{1}{3}}\overline{\boldsymbol{F}}, \tag{3.7}$$

where J is the Jacobian and $\overline{\boldsymbol{F}}$ is the deviatoric deformation gradient. Moreover, the elastic-viscous decomposition is used in the viscoelastic model:

$$\boldsymbol{F} = \boldsymbol{F}_e\boldsymbol{F}_v. \tag{3.8}$$

where $\boldsymbol{F}_e$ and $\boldsymbol{F}_v$ represent the elastic deformation and creeping viscous deformation, respectively. Then the energy rate can be expressed as

$$\begin{aligned} \dot{w} &= J^{-1}\boldsymbol{P} : \left(\frac{\partial}{\partial t}\left(J^{\frac{1}{3}}\right)\overline{\boldsymbol{F}} + J^{\frac{1}{3}}\dot{\overline{\boldsymbol{F}}}\right) \\ \dot{w} &= J^{-1}\boldsymbol{P} : \left(\dot{\boldsymbol{F}}_e\boldsymbol{F}_v + \boldsymbol{F}_e\dot{\boldsymbol{F}}_v\right) \end{aligned} \tag{3.9}$$

In these equations, the energy rate is separated into two terms that are not associated with one particular deformation. For example, the term $J^{-1}\boldsymbol{P} : \left(\frac{\partial}{\partial t}\left(J^{\frac{1}{3}}\right)\overline{\boldsymbol{F}}\right)$ is neither the volumetric energy rate nor the deviatoric energy rate because it is related

to both the volumetric deformation J and the deviatoric deformation $\overline{\boldsymbol{F}}$. The same conclusion applies to the second equation, the term $J^{-1}\boldsymbol{P} : \left(\dot{\boldsymbol{F}}_e\boldsymbol{F}_v\right)$ is neither the recoverable elastic energy rate nor the irrecoverable dissipated energy rate. However, it is important to divide the deformation into different modes associated with different energy form so that the stress can be computed accordingly. For the polyurea model, solving for the creep strain is critical for computing the energy dissipation and therefore it is important to remain the consistency between strain and energy.

Furthermore, the multiplicative decomposition has the non-uniqueness issue that has been mentioned in Chapter 1. Taking $\boldsymbol{F} = \boldsymbol{F}_e\boldsymbol{F}_v$ as an example, under an alternative observation frame, the three tensors can be transformed by the rotation tensor $\boldsymbol{Q}$ that is solely depending on the observation frame change and the multiplicative relation should remain unaltered.

$$\boldsymbol{F}^* = \boldsymbol{Q}\boldsymbol{F} = \boldsymbol{Q}\boldsymbol{F}_e\boldsymbol{Q}_x{}^T\boldsymbol{Q}_x\boldsymbol{F}_v \neq \boldsymbol{F}_e^*\boldsymbol{F}_v^* = \boldsymbol{Q}\boldsymbol{F}_e\boldsymbol{Q}\boldsymbol{F}_v \tag{3.10}$$

where $\boldsymbol{Q}_x$ is an arbitrary rotation tensor. Thus the solution for $\boldsymbol{Q}_x$ is non-unique. The consequences are that $\boldsymbol{F}_e^* = \boldsymbol{Q}\boldsymbol{F}_e\boldsymbol{Q}_x{}^T$ is not objective and $\boldsymbol{F}_v^* = \overline{\boldsymbol{Q}}\boldsymbol{F}_v$ can not be uniquely specified. A simple solution that assuming $\boldsymbol{Q}_x = \boldsymbol{I}$ would only be valid for isotropic materials. For materials like polyurea, which has a much stronger resistance in compression than tension, the constitutive models based on the assumption will not be objective. Another compromised solution is to neglect the rotational part in elastic deformation $\boldsymbol{F}_e = \boldsymbol{U}_e$ and therefore setting $\boldsymbol{Q}_x = \boldsymbol{Q}$ preserves the objectivity since $\boldsymbol{F}_e^* = \boldsymbol{Q}\boldsymbol{U}_e\boldsymbol{Q}^T = \boldsymbol{U}_e$. But ignoring the rigid body rotation can lead to an erroneous result when the elastic rigid body motion is large, which is the case for polyurea. Besides, this mathematical simplification actually assumes a stress-free intermediate configuration, which does not exist in reality. The rotational parts $\boldsymbol{R}_e$ and $\boldsymbol{R}_v$ should always be considered when building a constitutive model as the generic formulations

provided by Casey and Naghdi [48]. In which more complexity has been brought into the system and for a nonlinear model that contains properties from multiple constitutive laws such as a hyper-elastoplastic material, it becomes extremely difficult to obtain a strain or stress solution.

Additionally, for nonlinear FEM applications, a work-conjugate pair of Lagrangian measures is computed at the quadrature points. It is often necessary to recover the Cauchy stress from the undergoing variables to check the structural safety parameters or material status, such as checking von Mises stress. The traceless property of the deviatoric Cauchy stress will be lost during the transformation while using the multiplicative decomposition. For example, the deviatoric part of 2nd PK stress $\boldsymbol{S}$ is not traceless and can not transform to a traceless Cauchy stress. More detail about this issue will be shown in section 3.1.5.

3.1.2 Eulerian Description

To proceed with Eulerian strains and stresses is an alternative option. But there are many long existed problems and difficulties in developing Eulerian constitutive models. First of all, there is no simple and clear work-conjugate strain for Cauchy stress in Eulerian configuration. Starting from the energetic relation,

$$\dot{w} = \boldsymbol{\sigma} : \boldsymbol{D} \tag{3.11}$$

where $\dot{w}$ is the energy rate density and σ is the Cauchy stress. This relation is independent of notation or observation configuration.

If fixing a reference configuration, the same simple connection can be easily obtained, like the Green strain $\boldsymbol{E}$ and the 2nd Piola-Kirchhoff stress $\boldsymbol{S}$,

$$\dot{w} = J^{-1}\boldsymbol{S} : \dot{\boldsymbol{E}} \tag{3.12}$$

because we have the relationship between $\boldsymbol{D}$ and $\boldsymbol{E}$,

$$\boldsymbol{D} = \boldsymbol{F}^{-T} \cdot \dot{\boldsymbol{E}} \cdot \boldsymbol{F}^{-1}. \tag{3.13}$$

For Eulerian measures, it is difficult to relate $\boldsymbol{D}$ to the time derivative of a strain $\boldsymbol{\epsilon}$. Norris [77] presented generic solutions for the stresses conjugate to arbitrary Eulerian strains with extreme complexity.

The second difficulty is to define an objective rate of the strain measure (frame indifference). Because the measure is based on the current configuration, which is also in motion, the rates of Eulerian tensors are not objective. Letting $\dot{\boldsymbol{\epsilon}}$ be a Eulerian strain rate, then under a rotation of observer coordinate described by $\boldsymbol{Q}$, it is rewritten as:

$$\begin{aligned} \dot{\boldsymbol{\epsilon}}^* = \dot{\boldsymbol{\epsilon}^*} &= \dot{\overline{\boldsymbol{Q}\boldsymbol{\epsilon}\boldsymbol{Q}^T}} \\ &= \dot{\boldsymbol{Q}}\boldsymbol{\epsilon}\boldsymbol{Q}^T + \boldsymbol{Q}\dot{\boldsymbol{\epsilon}}\boldsymbol{Q}^T + \boldsymbol{Q}\boldsymbol{\epsilon}\dot{\boldsymbol{Q}}^T, \end{aligned} \tag{3.14}$$

which indicates that $\dot{\boldsymbol{\epsilon}}$ is obviously not objective. By using an objective rate measurement, e.g. the Jaumann rate $\boldsymbol{\epsilon}^J$, the objectivity can be retained

$$\begin{aligned} \overset{\triangledown J}{\boldsymbol{\epsilon}} &= \dot{\boldsymbol{\epsilon}} + \boldsymbol{\epsilon}\boldsymbol{W} - \boldsymbol{W}\epsilon \\ \left(\overset{\triangledown J}{\boldsymbol{\epsilon}}\right)^* &= \dot{\boldsymbol{\epsilon}^*} + \boldsymbol{\epsilon}^*\boldsymbol{W}^* - \boldsymbol{W}^*\epsilon^* \\ &= \boldsymbol{Q}\left(\dot{\boldsymbol{\epsilon}} + \boldsymbol{\epsilon}\boldsymbol{W} - \boldsymbol{W}\epsilon\right)\boldsymbol{Q}^T \\ &= \boldsymbol{Q}\overset{\triangledown J}{\boldsymbol{\epsilon}}\boldsymbol{Q}^T \end{aligned} \tag{3.15}$$

where $\boldsymbol{W}$ is the skew-symmetric part of velocity gradient $\boldsymbol{L}$.

3.1.3 Corotational Formulation

When building a constitutive model with the objective strain rates, with constant moduli, the objectivity requires the modulus matrix to be isotropic. For the Jaumann rate, a hypoelastic relation is

$$\overset{\triangledown J}{\boldsymbol{\tau}} = \boldsymbol{C}^{\tau J} : \boldsymbol{D} \tag{3.16}$$

and required to be objective:

$$\begin{aligned}\left(\overset{\triangledown J}{\boldsymbol{\tau}}\right)^* &= \boldsymbol{C}^{\tau J *} : \boldsymbol{D}^* \\ \boldsymbol{Q}\overset{\triangledown J}{\boldsymbol{\tau}}\boldsymbol{Q}^T &= \boldsymbol{C}^{\tau J} : \left(\boldsymbol{Q}\boldsymbol{D}\boldsymbol{Q}^T\right) \\ \overset{\triangledown J}{\tau}_{ij} &= Q_{mi}Q_{nj}Q_{pk}Q_{ql}C^{\tau J}_{mnpq}D_{kl} \\ &= C^{\tau J}_{ijkl}D_{kl}\end{aligned} \tag{3.17}$$

so

$$C^{\tau J}_{ijkl} = Q_{mi}Q_{nj}Q_{pk}Q_{ql}C^{\tau J} \tag{3.18}$$

for all rotations $\boldsymbol{Q}$, which leads to an isotropic $\boldsymbol{C}^{\tau J}$(see [78]).

A corotational formula is preferable for anisotropic materials since it does not have the limitation in moduli above. Let $\hat{\boldsymbol{\tau}}$ and $\hat{\boldsymbol{D}}$ denote the corotational Kirchhoff stress and deformation rate tensor. A hypoelastic relation is expressed as

$$\hat{\boldsymbol{\tau}} = \hat{\boldsymbol{C}}^{\tau} : \hat{\boldsymbol{D}} \tag{3.19}$$

where

$$\begin{aligned}\hat{\boldsymbol{\tau}} &= \boldsymbol{R}^T\boldsymbol{\tau}\boldsymbol{R} \\ \hat{\boldsymbol{D}} &= \boldsymbol{R}^T\boldsymbol{D}\boldsymbol{R}\end{aligned} \tag{3.20}$$

Follow the same procedure with Eq. (3.17) to check the objectivity,

$$(\hat{\boldsymbol{\tau}})^* = \boldsymbol{R}^{T*}\boldsymbol{\tau}^*\boldsymbol{R}^* = \boldsymbol{R}^T\boldsymbol{Q}^T\boldsymbol{Q}\boldsymbol{\tau}\boldsymbol{Q}^T\boldsymbol{Q}\boldsymbol{R} = \hat{\boldsymbol{\tau}} \tag{3.21}$$

and similarly $\hat{\boldsymbol{D}}^* = \hat{\boldsymbol{D}}$, the moduli is now not required to be isotropic. The corotational formula basically pulls the stress back by the rigid body rotation tensor $\boldsymbol{R}$ which is dependent on the observation coordinate. So the resulting stress tensor is independent of the rotation.

Additional issue arises that objective rates can not be exactly integrated for rate equation in 3.3, or even the simplest:

$$\hat{\boldsymbol{\sigma}}(t) = \int_0^t \dot{\hat{\boldsymbol{\sigma}}}(\tau)d\tau \tag{3.22}$$

where $\hat{\boldsymbol{\sigma}}$ is the corotational Cauchy stress (or Kirchhoff stress). This is known as the non-integrability of objective rates that first described by Simo and Pister [58]. Many of the commonly used objective rates including Jaumann rate, Green-Naghdi rate, Truesdell rate, and Oldroyd rate were examined and reported to have the issue. A more detailed example test will show this issue more clearly in section 3.1.5

3.1.4 Logarithmic Rate Formulation

Considering all the issues reviewed above, a logarithmic corotational formulation is selected to extend the polyurea constitutive model to finite strains. It is based on Eulerian configuration and was first presented by Xiao et al. [54] and showed intrinsic advantages on strain decomposition and without falling into the objectivity and integrability problem. According to the theory, the deformation rate tensor is a corotational rate form of Hencky strain:

$$\begin{aligned} \boldsymbol{D} &= (\ln \overset{\circ}{\boldsymbol{V}}) \\ &= \ln \dot{\boldsymbol{V}} + \ln \boldsymbol{V} \boldsymbol{\Omega}^{log} - \boldsymbol{\Omega}^{log} \ln \boldsymbol{V} \end{aligned} \tag{3.23}$$

with a unique choice of spin tensor $\boldsymbol{\Omega}^{log}$

$$\boldsymbol{\Omega}^{log} = \boldsymbol{W} + \boldsymbol{N}^{log} \tag{3.24}$$

where $\boldsymbol{N}^{log}$ is given as:

$$\boldsymbol{N}^{log} = \sum_{\substack{\alpha,\beta=1 \\ \alpha \neq \beta}}^{m} \left[\left(\frac{b_\alpha + b_\beta}{b_\beta - b_\alpha} + \frac{2}{\ln (b_\alpha / b_\beta)} \right) \boldsymbol{B}_\alpha \boldsymbol{D} \boldsymbol{B}_\beta \right] \tag{3.25}$$

This equation contains the m distinct eigenvalue of left tensor $\boldsymbol{B} = \boldsymbol{F}\boldsymbol{F}^T$, written as b_α and b_β. The α^{th} eigenprojection tensor $\boldsymbol{B}_\alpha$ is formed by outer product of two α^{th} eigenvectors

$$\boldsymbol{B}_\alpha = b_\alpha \boldsymbol{v}_\alpha \otimes \boldsymbol{v}_\alpha \qquad \text{or} \qquad B^\alpha_{ij} = b_\alpha v^\alpha_i v^\alpha_j \tag{3.26}$$

Note that in [54], the author further proved that the logarithmic strain is the only strain measure establishing the relation to the deformation rate tensor. It is also known that the deformation rate tensor and Cauchy stress form an energy conjugate pair. So the Hencky strain is the work-conjugate strain of Cauchy stress.

For convenience, the Hencky strain is hereafter denoted as ϵ_H. The spin tensor $\boldsymbol{\Omega}^{log}$ is called the logarithmic spin tensor and the mathematical proof is also given in the paper [54]. A rotation tensor can be derived from the logarithmic spin tensor is called the logarithmic rotation tensor:

$$\boldsymbol{Q}^{log} = -\boldsymbol{\Omega}^{log}\dot{\boldsymbol{Q}^{log}} \tag{3.27}$$

and it is called the logarithmic rotation tensor. The advantage of the logarithmic rotation is that the corresponding corotational form of $\boldsymbol{D}$ is exactly the material time derivative of Hencky strain

$$\begin{aligned}\hat{\boldsymbol{D}} &= (\boldsymbol{Q}^{log})^T\boldsymbol{D}\boldsymbol{Q}^{log} \\ &= (\boldsymbol{Q}^{log})^T\dot{\boldsymbol{\epsilon}_H}\boldsymbol{Q}^{log} + (\boldsymbol{Q}^{log})^T\boldsymbol{\epsilon}_H\dot{\boldsymbol{Q}^{log}} + (\dot{\boldsymbol{Q}^{log}})^T\boldsymbol{\epsilon}_H\boldsymbol{Q}^{log} \\ &= \overline{(\boldsymbol{Q}^{log})^T\dot{\boldsymbol{\epsilon}_H}\boldsymbol{Q}^{log}}\end{aligned} \tag{3.28}$$

Xiao et al. [54] also proved that no other objective rate formulation can establish such a convenient relationship between the deformation rate tensor and a strain measurement.

The above equation leads to a corotational form of Eq. (3.3) for large deformation:

$$\begin{aligned}\hat{\boldsymbol{\sigma}}'(t) &= \int_{-\infty}^{t} G(t-\tau)\hat{\boldsymbol{D}}'d\tau \\ (\boldsymbol{Q}^{log}_{(t)})^T\boldsymbol{\sigma}'(t)\boldsymbol{Q}^{log}_{(t)} &= \int_{-\infty}^{t} G(t-\tau)(\boldsymbol{Q}^{log}_{(\tau)})^T\boldsymbol{D}'\boldsymbol{Q}^{log}_{(\tau)}d\tau \\ \boldsymbol{\sigma}'(t) &= \boldsymbol{Q}^{log}_{(t)}\left[\int_{-\infty}^{t}(\boldsymbol{Q}^{log}_{(\tau)})^T G(t-\tau)\boldsymbol{D}'(\tau)\boldsymbol{Q}^{log}_{(\tau)}d\tau\right](\boldsymbol{Q}^{log}_{(t)})^T\end{aligned} \tag{3.29}$$

Xiao et al. [55, 57, 79–81] provided a detailed derivation of this logarithmic rate

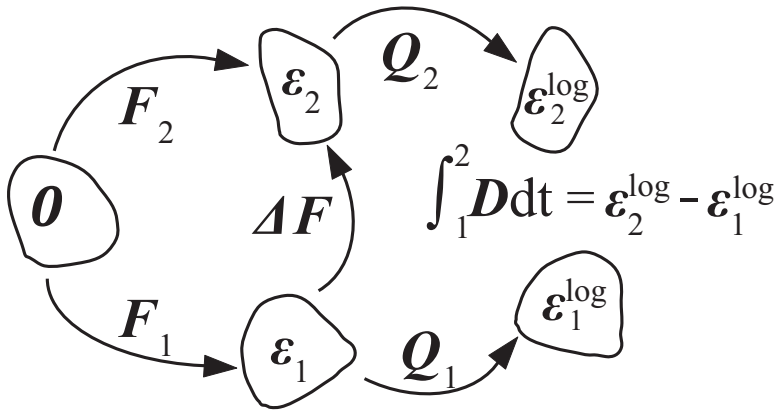

Figure 3.2: The logarithmic rotation finds an integrable intermediate configuration for the deformation decomposition by solving for $\boldsymbol{Q}$ in Eq. (3.27).

kinematic system and its good prospect of application for elastoplasticity and hypoelasticity problems.

A physical interpretation of the logarithmic rotation and the reason for these benefits it contains are shown in Figure 3.2. There exists a unique solution of rotation the matrix $\boldsymbol{Q}^{log}$ to transform the current configuration to a certain configuration such that the deformation rate tensor is identical to the rate of Hencky strain. This specific configuration is not a fixed configuration since $\boldsymbol{Q}^{log}$ is not only a function of deformation but also a function of deformation rate ($\boldsymbol{Q}^{log}(\boldsymbol{F}, \boldsymbol{D})$).

For our study, the logarithmic rate equation is embedded into the internal force integration where the Cauchy stress is always rotated by the logarithmic rotation tensor $\boldsymbol{Q}^{log}$ to a configuration such that the Hencky strain is integrable and additive decomposition of the strain holds. The update algorithm of $\boldsymbol{Q}^{log}$ follows the Hughes-Winget update described in [82] but uses a half step increment equation for $\boldsymbol{Q}$ to

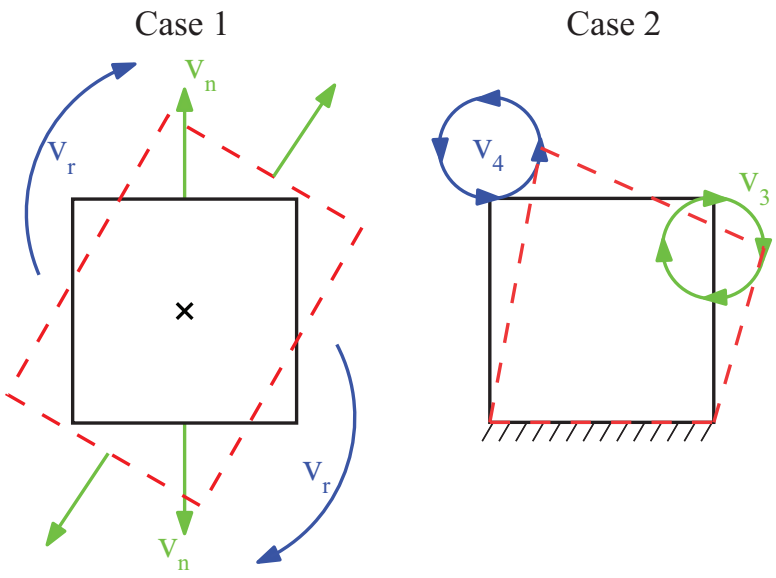

Figure 3.3: The element deformation is prescribed as case 1, rotation v_r plus uniform periodic elongation $v_n = A\sin(2\pi t)$, and case 2, top two nodes moving in circles.

conform to the leapfrog integration scheme used in integrating the nodal trajectories:

$$\begin{aligned} \dot{\boldsymbol{Q}}^{log} &= \boldsymbol{\Omega}^{log}\boldsymbol{Q}^{log} \\ \boldsymbol{Q}^{log}_{n+1/2} &= \boldsymbol{Q}^{log}_{n} + \frac{1}{2}\Delta t\boldsymbol{\Omega}^{log}_{n}\boldsymbol{Q}^{log}_{n} \\ \boldsymbol{Q}^{log}_{n+1} &= \boldsymbol{Q}^{log}_{n+1/2} + \frac{1}{2}\Delta t\boldsymbol{\Omega}^{log}_{n+1/2}\boldsymbol{Q}^{log}_{n+1/2} \end{aligned} \tag{3.30}$$

The benefits brought by this model such as additive decomposition, objectivity, direct Cauchy stress updates, and direct energy accumulation are at a limited amount of modifications to the small strain material model.

3.1.5 Performance of Different Rate Forms

A direct comparison between logarithmic rate and other rate forms is demonstrated. A linear elastic material element is deformed periodically in two different cases as shown in Figure 3.3. The stress evolution at one integration point is computed with different rate forms. Because no irrecoverable deformation happens in

linear elastic material, the residual stress after several complete cycles of deforming is expected to be zero or the rate form is not integrable. The test case 2 is similar to the test conducted in [83], but in our approach, only the deviatoric stress is computed, because 1) in the viscoelastic model only the shear stress is rate dependent, 2) the difference in deviatoric-volumetric decomposition by different integration schemes is of high interest: the trace of Cauchy stress should always be zero since the deviatoric stress should not be affected by volumetrical deformation.

$$\dot{\boldsymbol{\sigma}}' = G_0 \dot{\boldsymbol{\epsilon}}' \tag{3.31}$$

Additionally, a Lagrangian rate equation is also included in the comparison. In Lagrangian frame, a linear constitutive equation would be

$$\dot{\boldsymbol{S}} = \boldsymbol{C}^{SE} : \dot{\boldsymbol{E}} \tag{3.32}$$

in which $\boldsymbol{S}$ and $\boldsymbol{E}$ are the 2nd Piola-Kirchhoff stress and Green strain respectively. The deviatoric strain rate, denote as $\dot{\overline{\boldsymbol{E}}}$ requires some modifications:

$$\begin{aligned} \overline{\boldsymbol{F}} &= \boldsymbol{F} J^{-1/3} \\ \dot{\overline{\boldsymbol{E}}} &= \frac{1}{2}\left(\dot{\overline{\boldsymbol{F}}}^T \overline{\boldsymbol{F}} + \overline{\boldsymbol{F}}^T \dot{\overline{\boldsymbol{F}}}\right) \\ \dot{\overline{\boldsymbol{S}}} &= G_0 \dot{\overline{\boldsymbol{E}}} \end{aligned} \tag{3.33}$$

Finally the 2nd PK stress is transformed to Cauchy stress by

$$\overline{\boldsymbol{\sigma}} = J^{-1} \boldsymbol{F} \overline{\boldsymbol{S}} \boldsymbol{F}^T \tag{3.34}$$

where the isochoric Cauchy stress $\overline{\boldsymbol{\sigma}}$ is not traceless.

The results are shown in Figure 3.4 and 3.5. In case 1, there's hardly any difference between Eulerian frame rates (Logarithm, Jaumann, Green-Naghdi and Eulerian triad) and all rate equations preserve the integrability since the final stress returns to

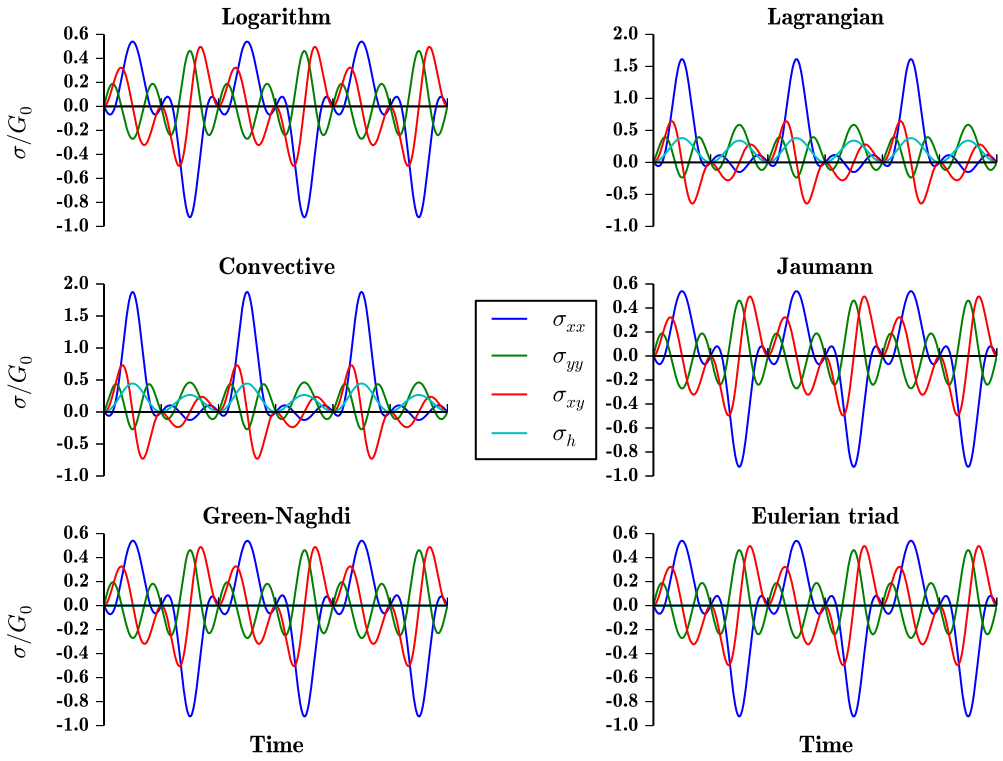

Figure 3.4: Stress history comparison between different rates in case 1.

zero. However, the hydrostatic stress $\boldsymbol{\sigma}_h$ of the Lagrangian frame is not always zero as expected. Indeed, the multiplicative deviatoric-volumetric decomposition can not perfectly recover the traceless isochoric Cauchy stress.

In case 2, as going through more complex deformation, all rate forms do not preserve integrability except logarithm and Lagrangian when looking at the residual stress. Lagrangian rate equations are of course always perfectly integrable because the reference configuration never changes. But the logarithmic rate as a Eulerian rate, besides offering a traceless isochoric stress tensor, also retains a very good integrability.

The above two cases well explain the advantage of logarithmic rate form. It

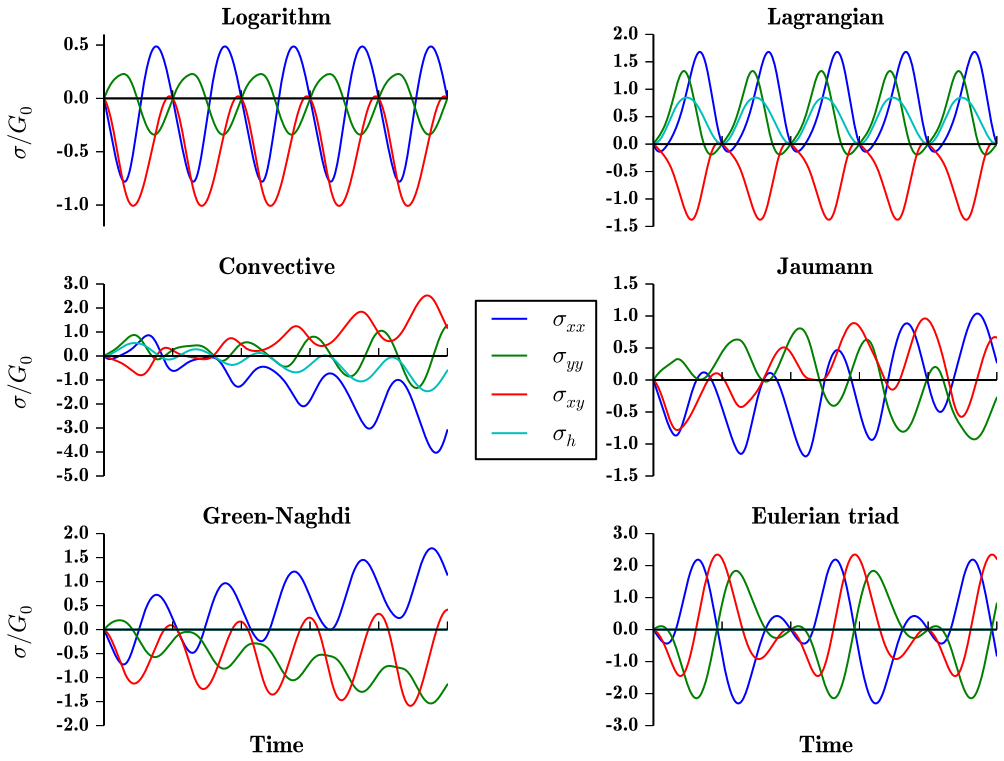

Figure 3.5: Stress history comparison between different rates in case 2.

automatically satisfies the objectivity and integrability conditions without rotating the variables back to reference configuration, which will eventually lead to a non-traceless Cauchy stress tensor. One can check other objective rates, but as proved in [54], the logarithmic rate is the only objective rate form that is integrable with a hypoelastic constitutive model.

For the application of the viscoelastic model, it is critical to directly check the objectivity of the logarithmic framework that whether it gives constant energy dissipation under rigid body rotation. So similar to test case 1, the material with the viscoelastic constitutive model is subjected to uniaxial stretch and rotation with different frequency. The uniaxial deformation is fixed and can be described by a pe-

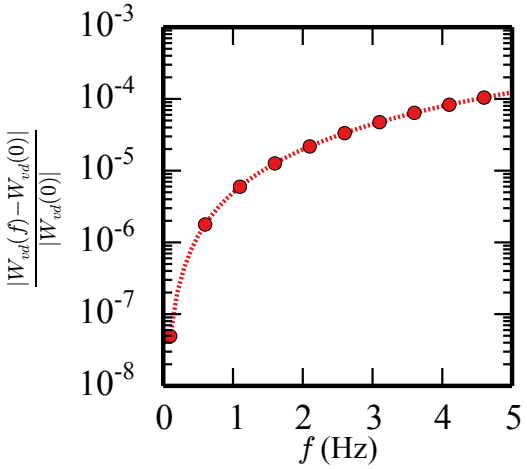

Figure 3.6: Error of dissipated energy under changing frequency of rigid body rotation.

riodical deformation gradient field where $F_{11} = 1.0 + A[1.0 - \cos(2\pi f_n t)]$. The rigid body rotation is applied by a rotation matrix:

$$\boldsymbol{R} = \begin{pmatrix} \cos(2\pi f t) & \sin(2\pi f t) \\ -\sin(2\pi f t) & \cos(2\pi f t) \end{pmatrix} \tag{3.35}$$

Then the motion of the material is described as $\boldsymbol{x} = \boldsymbol{R(t)F(t)X}$.

As the stress-strain response should be independent of the rigid body rotation, the dissipated energy should not change with different rotation frequency, i.e. $W_{vd}(f) = W_{vd}(0)\ \forall f$. So the normalized difference compared with the reference $W_{vd}(0)$ is plotted in frequency domain in Fig. 3.6. It shows that as the frequency increases, the loading speed is larger and the explicit system requires a smaller time step length. So using the same time step length in the test leads to a larger error in higher frequency. However, the change in the energy result is very small (and can be even smaller with a smaller time step length) throughout the frequency domain. This is a strong proof that the logarithmic rate form is objective and the energy integration does not depend on the rigid body rotation.

T_{ref}	273 (K)
B	184.64.53 (K)
A	-22.5
κ_{ref}	4.948 (GPa)
C_{te}	2×10^{-4} (K^{-1})
m	-0.015 (GPa K^{-1})
C_{tp}	7.2 (K GPa^{-1})

Table 3.1: Material parameters used in the constitutive model.

3.2 Viscoelastic Model

For the viscoelastic material model for polyurea, it is straightforward to expand the small deformation model to finite strain. Only two extra tensors to be computed at each step, the logarithmic spin tensor $\boldsymbol{\Omega}^{log}$ and rotation tensor $\boldsymbol{Q}^{log}$ and everything remains the same. It is necessary to note that the $\boldsymbol{Q}^{log}$ needs to be updated every time step as a material status. Moreover, the deformation inputs and stress outputs of the material subroutine all need to be rotated back and forth between the logarithmic configuration and current configuration. Within the material subroutine, since every variable is under the logarithmic configuration system, no tensor rotation need to be computed.

Since the magnitude of pressure wave generated by the surface loading is reduced both due to the viscosity of the coating and by stress reflection caused by the mismatched impedance between the substrate and the coating, the Plexiglas substrate is modeled as a simple elastic solid with Young's modulus $E = 2.4$ GPa, Poisson's ratio $\nu = 0.42$, and reference density $\rho = 1.18$ g/cm^3. All constants used in this model is summarized in 4.2.

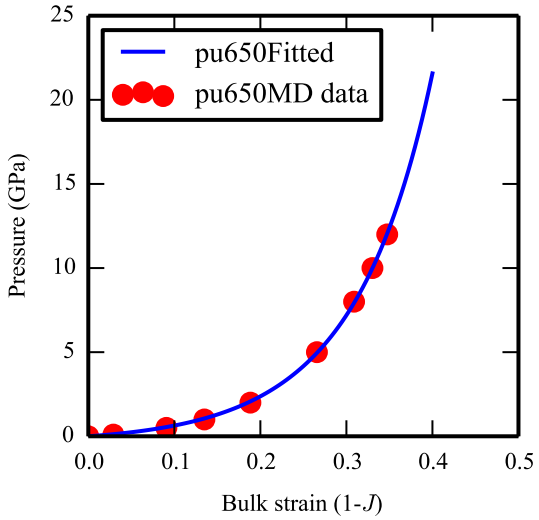

Figure 3.7: Fitting the molecular dynamics data with Lennard-Jones pressure model.

3.2.1 Volumetric Behavior

The coating is modeled as a viscoelastic solid using the Lennard-Jones type potential to describe the nonlinear pressure response:

$$p = -A\left(J_e^{-N-1} - J_e^{-M-1}\right), \tag{3.36}$$

where J_e is the Jacobian considering the thermal expansion coefficient α_V:

$$J_e = J[\alpha_V\,(T - T_0)]^{-3} \tag{3.37}$$

The constants of this model are fitted from atomistic molecular systems generated by Agrawal et al. [84] and listed in Table 3.2.

3.2.2 Deviatoric Response

The Prony series is used to simplify the nonlinear hereditary integration above. The material modulus relaxation during each characteristic time period is represented by an exponential function, which would vanish at a rate determined by q_i. Then the

	PU-650	PU-1000
A(GPa)	8.618	8.501
N	3.575	3.820
M	3.999	4.196

Table 3.2: Constants in Lennard-Jones pressure model.

overall relaxation function is expressed as a sum of the modulus of each Prony term.

$$G(t) = G_\infty \left(1 + \sum_{i=1}^{n} p_i e^{-t/q_i}\right) \tag{3.38}$$

where G_∞ is the fully relaxed shear modulus, q_i is the ith dissipation time scale and p_i is the ith relative weight of shear modulus.

In order to obtain the material constants from DMA (Dynamic Mechanical Analysis) test, the relaxation function is expressed in the frequency domain.

$$G'(\omega) = G_\infty \left(1 + \sum_{i=1}^{n} p_i \frac{\omega^2 q_i^2}{1+\omega^2 q_i^2}\right) \tag{3.39}$$

$$G''(\omega) = G_\infty \sum_{i=1}^{n} p_i \frac{\omega q_i}{1+\omega^2 q_i^2} \tag{3.40}$$

Jia et al. [85] extracted the master curves of storage modulus G' and loss modulus G'' from DMA test of PU-1000 using time-temperature superposition. In order to get a higher frequency response, we fitted the master curves of PU-650 and PU-1000 provided by them using 9 and 10 Prony terms respectively. The fitting is plotted in Fig. 3.8 and the resulting constants are listed in Table 3.3.

Temperature effect on polyurea's dynamic properties has been considered in this model. Above the glass transition temperature $T_g = -50°$C, polyurea under lower frequency loading behaves similarly with under higher temperature. Therefore an empirical correlation between its temperature response and frequency response can

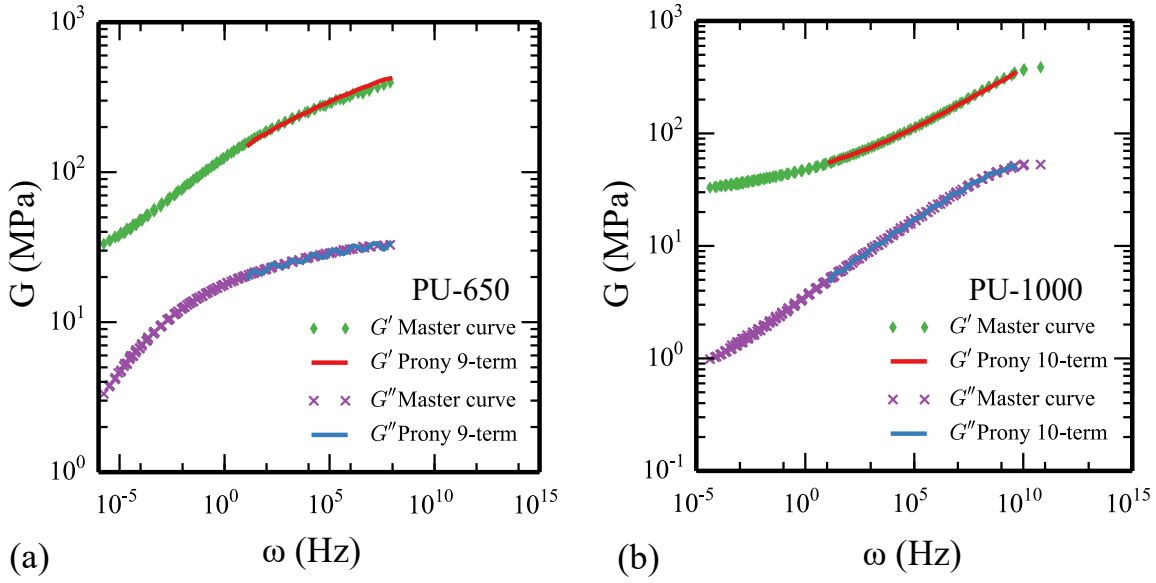

Figure 3.8: Fitting master curves of storage modulus and loss modulus.

be described as a shifting function of temperature in frequency domain [86]:

$$\omega_r = a(T)\omega \tag{3.41}$$

where ω_r is the reduced frequency and $a(T)$ is the frequency shifting function. This time-temperature shifting property is widely used to learn the dynamic property of polyurea in the frequency domain by testing it under different temperature since directly applying wide range frequency condition is very challenging. It is validated by Zhao et. al [87] that the time-temperature superposition principle used in classic viscoelastic material models is still valid at various temperatures. The frequency shifting factor can be computed according to Knauss et al. [88]:

$$a = 10^{A(T-T_{ref})/(B+(T-T_{ref}))} \tag{3.42}$$

Since polyurea is also sensitive to pressure, its pressure dependence is represented by introducing a time-pressure coefficient C_{tp} which can be obtained experimentally.

$$T(t,p) = T(t) - C_{tp}p \tag{3.43}$$

PU-1000		PU-650	
$G_\infty = 52.79$ MPa		$G_\infty = 139.06$ MPa	
p_i	q_i (s)	p_i	q_i (s)
1.705	3.063×10^{-10}	0.714	2.712×10^{-11}
1.106	2.929×10^{-9}	0.715	3.292×10^{-9}
0.873	2.307×10^{-8}	0.352	6.947×10^{-8}
0.700	1.872×10^{-7}	0.323	6.837×10^{-7}
0.516	1.457×10^{-6}	0.299	6.558×10^{-6}
0.400	1.083×10^{-5}	0.279	6.129×10^{-5}
0.313	8.242×10^{-5}	0.251	5.620×10^{-4}
0.241	6.487×10^{-4}	0.242	5.128×10^{-3}
0.182	5.213×10^{-3}	0.258	5.306×10^{-2}
0.167	4.766×10^{-2}		

Table 3.3: Relaxation time scales and their corresponding shear moduli.

This linear shifting in temperature effectively describes the glass-like hardening behavior of polyurea under large pressure and greatly satisfies the need of modeling high-pressure bubble collapsing loading.

In the material model, the time-temperature shifting factor is regarded as a delay in material property change, in other words, the time variable in the constitutive subroutine is scaled to a new timeline by the integration expression:

$$\xi(t) = \int_0^t \frac{d\tau}{a(T(\tau), T_0)} \tag{3.44}$$

where $\xi(t)$ is the new time frame that the material properties are changing with.

By the logarithm rate equations, the simplicity of Eq. (3.3) is preserved while con-

forming with large rotation. Also, the deviatoric part of stress derived in Eq. (3.1) is remained to be isochoric. More importantly, it maintains the additive decomposition in elastic-viscous and elastic-plastic split from energy rate point of view.

$$\dot{W} = \boldsymbol{\sigma} : \boldsymbol{D} = \dot{W}_e + \dot{W}_v \tag{3.45}$$

and then $\boldsymbol{D}_e$ and $\boldsymbol{D}_v$ are introduced such that

$$\dot{W}_e = \boldsymbol{\sigma} : \boldsymbol{D}_e, \quad \dot{W}_v = \boldsymbol{\sigma} : \boldsymbol{D}_v \tag{3.46}$$

The sub-deformation rate $\boldsymbol{D}_e$ and $\boldsymbol{D}_v$ contributes to recoverable elastic energy and irrecoverable viscous energy respectively.

Substituting Eq. (3.38) into Eq. (3.3) and apply the time-temperature shifting factor, we have

$$\hat{\boldsymbol{\sigma}}' = \int_{-\infty}^{t} G_\infty \left(1 + \sum_{i=1}^{n} p_i e^{-(\xi(t)-\xi(\tau))/q_i}\right) \hat{\boldsymbol{D}}' d\tau \tag{3.47}$$

Taking one of the spring-dashpot element from the Maxwell-Wiechert model in Fig. 3.1 into consideration, the stress $\boldsymbol{\sigma}^i$ is solely provided by the elastic spring that being stretched by a strain of $\boldsymbol{\epsilon}_e^i$ and a strain rate $\hat{\boldsymbol{D}}_e$. From Eq. (3.47), we already know that the stress on the single element is

$$\begin{aligned} \hat{\boldsymbol{\sigma}}^{i\prime} &= \int_{-\infty}^{t} G_\infty p_i e^{-(\xi(t)-\xi(\tau))/q_i} \hat{\boldsymbol{D}}' d\tau \\ \hat{\boldsymbol{\sigma}}^{i\prime} &= G_\infty p_i \int_{-\infty}^{t} e^{-(\xi(t)-\xi(\tau))/q_i} \hat{\boldsymbol{D}}' d\tau \end{aligned} \tag{3.48}$$

and therefore the elastic strain is obtained accordingly:

$$\hat{\boldsymbol{\epsilon}}_e^{i\prime} = \int_{-\infty}^{t} e^{-(\xi(t)-\xi(\tau))/q_i} \hat{\boldsymbol{D}}' d\tau \tag{3.49}$$

Then according to the additive decomposition, the viscous strain (creep strains) can be expressed by the exponential forms as

$$\hat{\boldsymbol{\epsilon}}_v^{i\prime} = \hat{\boldsymbol{\epsilon}}' - \hat{\boldsymbol{\epsilon}}_e^{i\prime} = \int_{\infty}^{t} \left(1 - e^{-(\xi(t)-\xi(\tau))/q_i}\right) \hat{\boldsymbol{D}}' d\tau \tag{3.50}$$

Here $\hat{\boldsymbol{\epsilon}}'$ is the logarithmic form of the deviatoric Hencky strain $(\boldsymbol{Q}^{log})^T \boldsymbol{\epsilon}_H \boldsymbol{Q}^{log}$ and $\hat{\boldsymbol{D}}' = (\boldsymbol{Q}^{log})^T \boldsymbol{D}' \boldsymbol{Q}^{log}$.

Then the recursive increment of creep strain can be solved explicitly in each loading step:

$$\Delta\hat{\boldsymbol{\epsilon}}_v^i(t,\Delta t) = (1-e^{-\Delta\xi/q_i})\left(\hat{\boldsymbol{\epsilon}}'(t) - \hat{\boldsymbol{\epsilon}}_v^i(t)\right) + \left(1 - \frac{q_i}{\Delta\xi}(1-e^{-\Delta\xi/q_i})\right)\hat{\boldsymbol{D}}'(t)\Delta t \quad (3.51)$$

where $\Delta\xi$ denotes $\xi(t) - \xi(\tau)$ for convenience.

Finally, the dissipated energy is computed as a portion of the elastic energy and the ratio is just the retardation time for each sub-element:

$$\frac{\partial W_d^i}{\partial t} = \sum_{i=1}^{n} \boldsymbol{\sigma}^{i\prime} : \boldsymbol{D}_v^{i\prime} \quad (3.52)$$

$$= \sum_{i=1}^{n} \frac{1}{q^i}\boldsymbol{\sigma}^{i\prime} : \boldsymbol{\epsilon}_e^{i\prime} \quad (3.53)$$

$$= 2G_\infty \frac{T}{T_{ref}} \sum_{i=1}^{n} \frac{p_i}{q_i}(\boldsymbol{\epsilon}' - \boldsymbol{\epsilon}_v^{i\prime}) : (\boldsymbol{\epsilon}' - \boldsymbol{\epsilon}_v^{i\prime}) \quad (3.54)$$

and the raise of temperature is determined directly from dissipated energy by a linear equation:

$$\frac{\partial T}{\partial t} = \frac{1}{C}\frac{\partial W_d}{\partial t} \quad (3.55)$$

where C is the heat capacity at constant volume per unit of original volume.

Stress can be obtained straightforwardly now

$$\sigma'(t) = 2G_\infty \left(\epsilon'(t) + \sum_{i=1}^{n} p_i \epsilon_e^i(t)\right) \quad (3.56)$$

A nonlinear solver is required to obtain the recursive temperature changing. We implemented a binary search based algorithm in the constitutive subroutine, which has a first order convergence rate. However, since the FEM system is dynamic and the bubble collapse loads are usually of extremely short duration, the time increment is limited to extremely small (usually less than 10 nanoseconds for a reasonably fine

mesh). So the temperature increment in each step is small and the binary searching range is narrow: it converges to less than 0.01% error in 10 iterations. We summarize the algorithm to update the stress including the logarithmic co-rotational transformation as below:

3.3 Deformation-dependent Stress Response

The fact that the large stretch response of rubber materials is not simple linear elastic is already widely observed and proved. Stress softening around 10% strain and hardening at large strains is observed in the experiments conducted by different groups [45, 89, 90]. So a more elaborate nonlinear hyperelastic model is needed to represent these characteristics of polyurea. As suggested in [45], the 8-chain network model by Arruda and Boyce [59, 91, 92] is embedded in the elastic component to address the hyperelastic stress hardening at large deformation. Additionally, a simple power law plastic model is also used to describe the material softening, or the Mullins effect. This new model will be able to capture the characteristics of polyurea:

- Objective, stable, and accuratestress integration.
- Pressure and strain rate dependent thermal dissipation and viscosity.
- Deformation dependent nonlinear response in large deformation.

A preliminary result of this nonlinear model is shown to illustrate its capability of modeling the material behavior under various load circumstances. However, due to the lack of experimental data to validate the model, especially the results of the thermal properties of polyurea, this section only presents the framework of the nonlinear model and the parameters are not rigorously selected or fitted.

Algorithm 1: Co-rotational Stress Update Algorithm

For every time increment from t_n to t_{n+1}:

A. **Obtain co-rotational forms:**

(a) Compute $\boldsymbol{D}_{n+\frac{1}{2}}$, $\boldsymbol{W}_{n+\frac{1}{2}}$, and $\boldsymbol{F}_{n+\frac{1}{2}}$ from $\boldsymbol{u}_{n+\frac{1}{2}}$ and $\boldsymbol{v}_{n+\frac{1}{2}}$

(b) Compute $\boldsymbol{\Omega}^{log}_{n+\frac{1}{2}}$ and update $\boldsymbol{Q}^{log}_{n}$ to $\boldsymbol{Q}^{log}_{n+\frac{1}{2}}$ (Eq. (3.24) and 3.30)

(c) Update the variables to co-rotational forms by $\hat{(*)} = \boldsymbol{Q}^{logT}_{n+\frac{1}{2}}(*)\boldsymbol{Q}^{log}_{n+\frac{1}{2}}$

B. **Constitutive relations:**

(a) Initiate the range of ΔT: $[\Delta T^{guess}_{lo}, \Delta T^{guess}_{up}]$

(b) Solve for ΔT recursively:

i. Set trial solution $\Delta T^{guess} = 0.5(\Delta T^{guess}_{hi} + \Delta T^{guess}_{lo})$

ii. Compute p_{n+1} (Eq. (3.36))

iii. Compute $\dot{W}_v$ (Eq. (3.54))

iv. Initiate the range of $\Delta\hat{\boldsymbol{\epsilon}}_p$: $[\Delta\hat{\boldsymbol{\epsilon}}^{guess}_{p,lo}, \Delta\hat{\boldsymbol{\epsilon}}^{guess}_{p,up}]$

v. Solve for $\Delta\hat{\boldsymbol{\epsilon}}_p$ recursively:

1. Set trial solution $\Delta\hat{\boldsymbol{\epsilon}}^{guess}_{p} = 0.5(\Delta\hat{\boldsymbol{\epsilon}}^{guess}_{p,lo} + \Delta\hat{\boldsymbol{\epsilon}}^{guess}_{p,up})$

2. Check the error of $\hat{\boldsymbol{\epsilon}}^{guess}_{p}$ (Eq. (3.62))

3. If convered: quit; else: update $\Delta\hat{\boldsymbol{\epsilon}}^{guess}_{p,lo}$ or $\Delta\hat{\boldsymbol{\epsilon}}^{guess}_{p,up}$ and go to 1.

vi. Compute $\dot{W}_p$ (Eq. (3.65))

vii. Check the error of T^{guess} (Eq. (3.55))

viii. If converged: quit; else: update ΔT^{guess}_{lo} or ΔT^{guess}_{up} and go to i.

(c) Update: $\hat{\boldsymbol{\sigma}}_n \to \hat{\boldsymbol{\sigma}}_{n+1}$, $\hat{\boldsymbol{\epsilon}}_{p,n} \to \hat{\boldsymbol{\epsilon}}_{p,n+1}$, $\hat{\boldsymbol{\epsilon}}_{c,n} \to \hat{\boldsymbol{\epsilon}}_{c,n+1}$

C. Convert the stress back to global coordinate $\boldsymbol{\sigma} = \boldsymbol{Q}^{log}\hat{\boldsymbol{\sigma}}\boldsymbol{Q}^{logT}$

D. Update $\boldsymbol{Q}^{log}_{n+\frac{1}{2}}$ to $\boldsymbol{Q}^{log}_{n+1}$ (Eq. (3.30))

3.3.1 Hyperelastic Model

In Arruda-Boyce model, a strain energy function based on the Langevin chain statistics is expressed in terms of macro-scale stretch invariant. The Langevin expression of strain energy is

$$\begin{aligned} W &= nkT\left[\sqrt{N}\lambda_{chain}\beta + N\ln\frac{\beta}{\sinh\beta}\right], \\ \beta &= \mathcal{L}^{-1}\left(\frac{\lambda_{chain}}{\sqrt{N}}\right) \end{aligned} \tag{3.57}$$

where $\mathcal{L}^{-1}$ is the inverse of the Langevin function. The λ_{chain} is an averaged stretch of the chains that can be computed by $\lambda_{chain} = \sqrt{\frac{1}{3}\text{trace}(\boldsymbol{B})}$. The product of the chain density n, Boltzmann's constant k, and temperature T can be replaced by the instantaneous shear modulus G_0 at stress-free state. The constant N is the number of Kuhn lengths in the molecular chain. So in total only two material constants, which both have actual physical meaning, are required in this model which makes it more concise. Using the series expansion of the inverse Langevin function, the first 5 terms can be written as:

$$\begin{aligned} W(I_1) = nkT\Bigg[&\frac{1}{2}(I_1-3) + \frac{1}{20N}(I_1^2-9) + \frac{11}{1050N^2}(I_1^3-27) \\ &+\frac{19}{7000N^3}(I_1^4-81) + \frac{519}{673750N^4}(I_1^5-243)\Bigg] \end{aligned} \tag{3.58}$$

where I_1 is the first invariant of left tensor $\boldsymbol{B}$ and $\lambda_{chain} = \sqrt{\frac{1}{3}I_1}$. Taking the derivative of this energy expression, the deviatoric Cauchy stress is obtained as:

$$\boldsymbol{\sigma}' = 2\frac{dW}{dI_1}\boldsymbol{B}' \tag{3.59}$$

where $\boldsymbol{B}'$ is the left tensor derived from traceless Hencky strain $\boldsymbol{\epsilon}'$ such that $(\det(\boldsymbol{B}) = 1)$. Then the strain dependent stress relation is built

$$\boldsymbol{\sigma}'(\boldsymbol{B}) = \frac{G_0\sqrt{N}}{\sqrt{3I_1}}\mathcal{L}^{-1}\left(\sqrt{\frac{I_1}{3N}}\right)\boldsymbol{B}' \tag{3.60}$$

where the Langevin inverse can be simply approximated as

$$\mathcal{L}^{-1}\left(\sqrt{\frac{I_1}{3N}}\right) \approx \sqrt{\frac{I_1}{3N}}\frac{3-\frac{I_1}{3N}}{1-\frac{I_1}{3N}} \tag{3.61}$$

3.3.2 Plastic Model

The long-term stress response $\boldsymbol{\sigma}_\infty$ is further coupled with a Ramberg-Osgood plasticity formula to account for the damage within the material:

$$\overline{\epsilon}^p = \alpha\epsilon_y\left(\frac{\overline{\sigma}_\infty}{\sigma_y}\right)^n \tag{3.62}$$

where $\overline{\sigma}_\infty$ is the von Mises stress of the long-term response, which is computed by the hyperelastic stress formula in Eq. (3.60) using the elastic strain $\boldsymbol{\epsilon}^e = \boldsymbol{\epsilon} - \boldsymbol{\epsilon}^p$. α and n are the material constants determining the hardening behavior of the material. $\overline{\epsilon}^p_y$ is the effective plastic strain that needs to be solved each step. The yield stress is assumed to change with temperature, according to [40]:

$$\sigma_y(T) = \sigma_{y0}\left(1-\frac{T-T_0}{T_m-T_0}\right)^l \tag{3.63}$$

where σ_{y0} is the initial yielding stress and is associated with the initial yielding strain ϵ_{y0}, which is assumed to be 3%. The T_m and l are the melting temperature and the thermal softening exponent, respectively. Therefore the plastic strain is also related to the temperature and therefore must be solved in a sub-loop of the aforementioned temperature solver. Additionally, since the elastic region is described by the hyperelastic formula, a nonlinear solver is needed to obtain the effective plastic strain. The binary search algorithm is adopted in this work to solve for the plastic strain. The estimated constants are listed in Table 3.4.

3.3.3 Coupled Formulation

The combination of the two models can be interpreted as replacing the linear elastic springs in Fig. 3.1 by Arruda-Boyce deformation-dependent hyperelastic springs

N	n	l	α	ϵ_{y0}	T_m (K)
4.0	8	0.75	0.33	0.03	500

Table 3.4: Constants in the nonlinear model including hyperelasticity and plasticity.

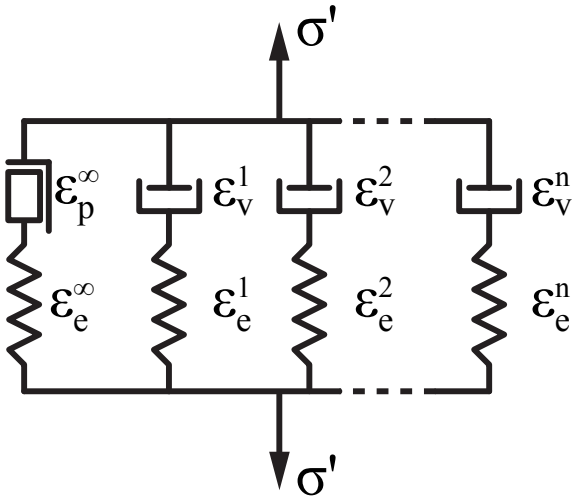

Figure 3.9: Illustration of viscoelastic model coupled with deformation dependent hyperelastic and power law plastic models.

and adding a plastic module to the static subelement, as shown in Fig. 3.9. Since the additive strain decomposition is still valid and the strain is integrable, the elastic strain $\boldsymbol{\epsilon}'_e$ in each sub-element can be easily computed cumulatively and a $\boldsymbol{B}'_e$ matrix associated with the elastic deformation is obtained according to the definition of Hencky strain $\boldsymbol{\epsilon}'_e = (\ln \boldsymbol{V}')_e$:

$$\boldsymbol{\sigma}^{i\prime}(\boldsymbol{B}_e^{i\prime}) = \frac{G_\infty T p_i \sqrt{N}}{T_{ref}\sqrt{3I_1^i}} \mathcal{L}^{-1}\left(\sqrt{\frac{I_1^i}{3N}}\right) \boldsymbol{B}_e^{i\prime} \tag{3.64}$$

in which the stress of each spring is now a function of the current deformation state, $\boldsymbol{\sigma}^{i\prime}(\boldsymbol{B}_e^{i\prime})$, while still linearly scaled by the temperature.

Beside the viscous energy dissipation given by Eq. (3.54), a portion of the work done by the static stress is also dissipated into heat due to the plastic strain. So the

expression of dissipated energy is rewritten as:

$$\begin{aligned}\dot{W}_d &= \dot{W}_v + \dot{W}_p \\ &= \sum_{i=1}^{n} \frac{1}{q^i} \boldsymbol{\sigma}^{i\prime}(\boldsymbol{B}_e^{i\prime}) : \boldsymbol{\epsilon}_e^{i\prime} + \boldsymbol{\sigma}_\infty : (\dot{\boldsymbol{\epsilon}} - \dot{\boldsymbol{\epsilon}}^p)\end{aligned} \tag{3.65}$$

This expression gives a more comprehensive description of the heating within the material by including the plastic energy. In fact, under large deformation, the plastic dissipation, thus the damage within the material, is the dominant resource of the heating.

The deviatoric stress is a sum of all stresses associated with different frequency and the static stress term results from plastic model:

$$\boldsymbol{\sigma}'(\boldsymbol{B}) = \boldsymbol{\sigma}'_\infty(\boldsymbol{B}', T) + \sum_{i=1}^{n} \boldsymbol{\sigma}^{i\prime}(\boldsymbol{B}_e^{i\prime}) \tag{3.66}$$

Comparing this nonlinear hyperelastic stress equation with linear equation elastic equation in Eq. (3.56), the stress is now not only a function of time but also a function of the deformation. In compression, due to the nonlinear relation with deformation in the hyperelastic model, the model presents a stiffer material behavior than before and better describes the stiffening behavior of polyurea under large deformation.

In fact, both volumetric and deviatoric plasticity exist in polyurea. According to studies of crystalline polymers [93–95], the volumetric plasticity is generated when the polymer is subjected to large negative pressure. For polyurea, since it is less resistant in tension than in compression, the negative pressure load is very likely to generate hydrostatic damage. In the application of liquid cavitation loading, since the majority material is under compression and the tension stress in partial area is small, only deviatoric plasticity is considered. However, it is highly interested to find a more comprehensive plastic model with the description of the volumetric damage, e.g. the Gurson model with porosity evolution. Moreover, the power law plastic model is not

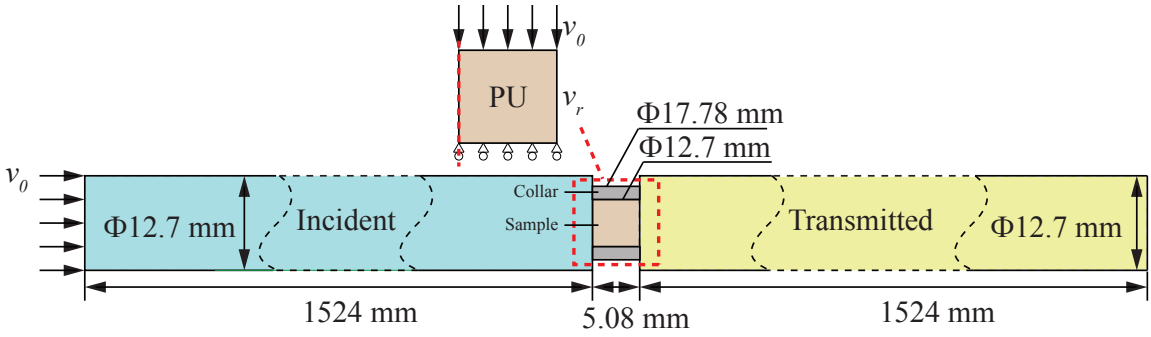

Figure 3.10: The Hopkinson pressure bar test and the simplified numerical model.

based on the underlying microstructural process in the material. It is a mathematical approximation in order to capture the stress softening of the polyurea, so the material constants are essentially fitted from experimental results and can hardly be a general formula.

3.3.4 Preliminary Results

With the Hopkinson pressure bar test data from UCSD's CEAM [45], we briefly examined the performance of the new nonlinear model. As shown in Fig. 3.10, the Hopkinson bar test is simplified to a cylindrical material subjected to a constant velocity v_0 in our axisymmetric FEM platform. Since the impedance of polyurea is small compared with the incident and transmitted bars, which are made of steel, the particle velocity of the shock load is assumed to be fully transmitted to polyurea sample and keeps constant during the sample deformation. Moreover, the surface contacting the transmitted bar is assumed constraint.

Two sets of experiments have been done, one with the collar confining the sample, and the other without the collar. For the confined experiment, due to the large resistant force from the sample, a noticeable hoop strain in the collar is observed. So the hoop strain $\epsilon_{\theta\theta}$ is measured by strain gauges on the outer surface and a moving

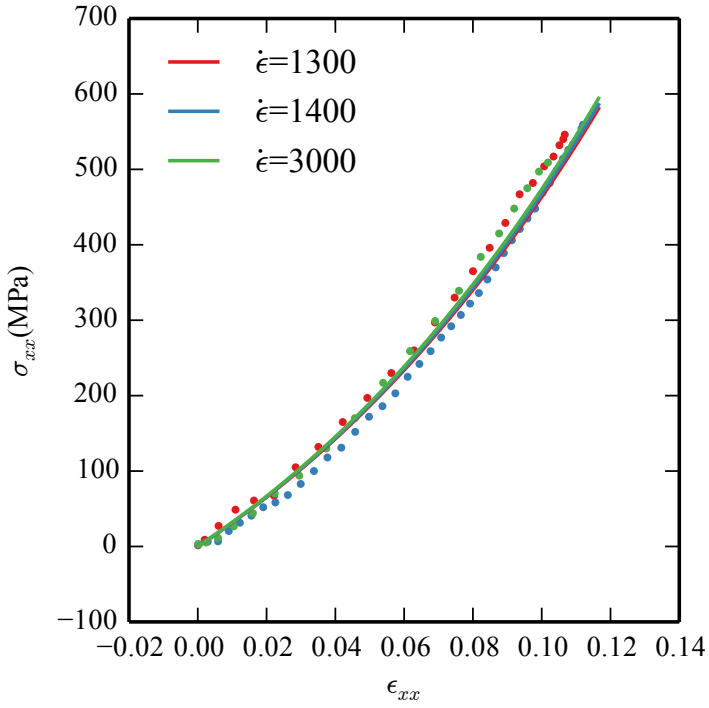

Figure 3.11: The stress-strain relationship at different strain rates from numerical model and the confined experiment.

boundary with an averaged velocity v_r is defined:

$$v_r = \frac{\epsilon_{\theta\theta} r}{\Delta t} \tag{3.67}$$

where r is the radius and Δt is the total time. For the unconfined experiment, the right boundary is a free surface.

Fig. 3.11 shows the stress-strain relationship predicted by the nonlinear material model. Although the radial expansion of the sample is considered, it is very small compared with uniaxial deformation. So significant volumetric deformation takes place and the resulting pressure becomes the main resource of uniaxial stress, thus the stress triaxiality is large. Because the pressure response of polyurea is not rate-dependent, as introduced in section 3.2.1, the stress-strain curves under different

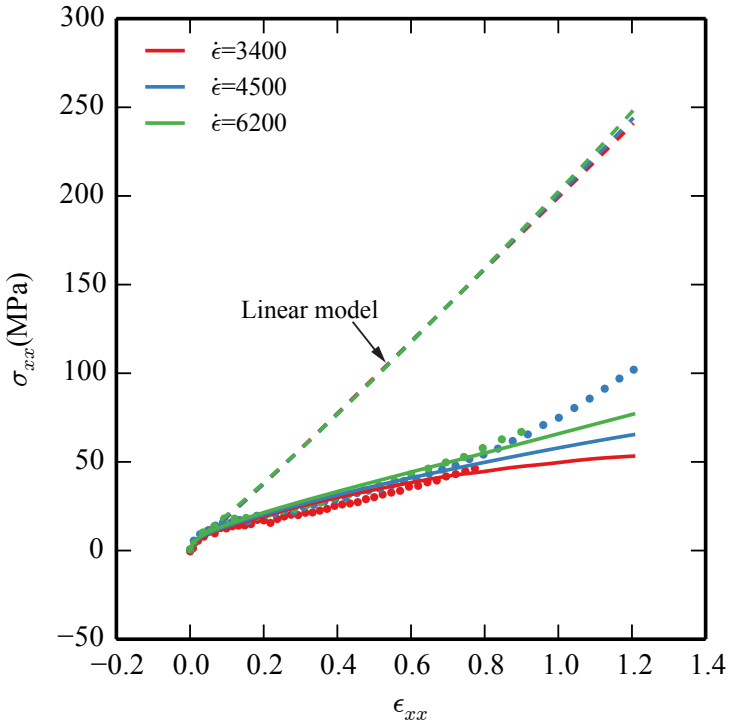

Figure 3.12: The stress-strain relationship at different strain rates from the numerical model and the unconfined experiment

strain rates are similar. The numerical result matches the experimental data very well, indicating that the pressure law is reliable and accurate.

In Fig. 3.12, both the linear viscoelastic model and the augmented hyper-viscoplastic model are compared with the experimental data. Without the collar, the sample expands freely in the radial direction and the material is nearly incompressible due to the stiff volumetrical deformation resistance of polyurea. Then the uniaxial stress mainly comes from the deviatoric stress, thus the shear response of polyurea. The initial slope of the stress-strain curve, i.e. the instantaneous shear modulus, from the linear model matches with the experiments very well, which is consistent with the work by Amirkhizi et al. [45]. The nonlinear model successfully retains the ac-

curacy within small strain while provides more realistic prediction at larger strains. The stress is softened around 10% strain and slightly hardened at large deformation. With increasing strain rates, the nonlinear model also generates a higher stress. In general, the same trend of the stress-strain relationship is produced by the nonlinear model.

Again the model is not rigorously calibrated with sufficient experimental data. The results shown here is just to verify the framework is capturing the correct trend of the polyurea behavior. Since the behavior of polyurea under large deformation is highly nonlinear, characterized by temperature dependent, pressure dependent, hysteresis, plasticity, hyperelasticity, and rate dependent, it is highly interested to build a constitutive law capturing all these properties while accounting for the microstructural behaviors. The existing Amirkhizi model and Arruda-Boyce model are the good examples of such constitutive laws but emphasize on parts of the many characteristics: temperature, pressure effects and thermal behavior by Amirkhizi model and stretch-induced stress hardening by Arruda-Boyce model. A more sophisticated plastic model is needed to enrich the model with description permanent strain evolution.

As a summary of this chapter, the kinematics of large deformation for constructing constitutive models for polyurea have been disscussed and the logarithmic corotational formulation is embedded in the Amirkhizi viscoelastic model. Test cases are also given to show the integrability and objectivity of logarithmic rate. Augmented constitutive model with stretch-dependent Arruda-Boyce hyperelastic model and temperature dependent Ramberg-Osgood plastic model is shown as a prospective framework to describe the response of polyurea in large deformation.

Chapter 4

FINITE ELEMENT MODELING

4.1 FEM Model

The transmission and dissipation of the representative hydrodynamic bubble collapse loads are modeled by a finite element simulation. The objective of this FE model is to precisely calculate the energy dissipation within the coating under a single bubble collapse load. Because the statistical integration of the heating energy is based on the FE results of the sampled impact loads, the accuracy of the FE model is critical. Nevertheless, since a large number of sampling simulations are needed for different thickness, material, and cavitating environments, the efficiency of each simulation is also important.

A schematic of the model is shown in Fig. 4.1. The simulation domain is a cylindrical region of the coated plate specimen, centered directly under a collapsing bubble. The simulation domain has a radius of 2 mm and extends 2 mm into the depth of the substrate. The radius of the specimen, which is the domain width, and the height of the substrate, are large enough so that the stress wave arriving at the boundary is suppressed.

The domain is discretized by quadrilateral elements with an edge length of 20 μm. The elements are first order quadrilateral elements with 4 Gaussian integration points. Uniform mesh is used in this study as the geometry is simple. Since the radius of a small bubble collapse load is as small as 50 μm, the element size is very limited in order to capture the spatial distribution of the load. As shown in Fig. 4.2, for a small bubble collapse load, a coarse mesh can not provide enough resolution to

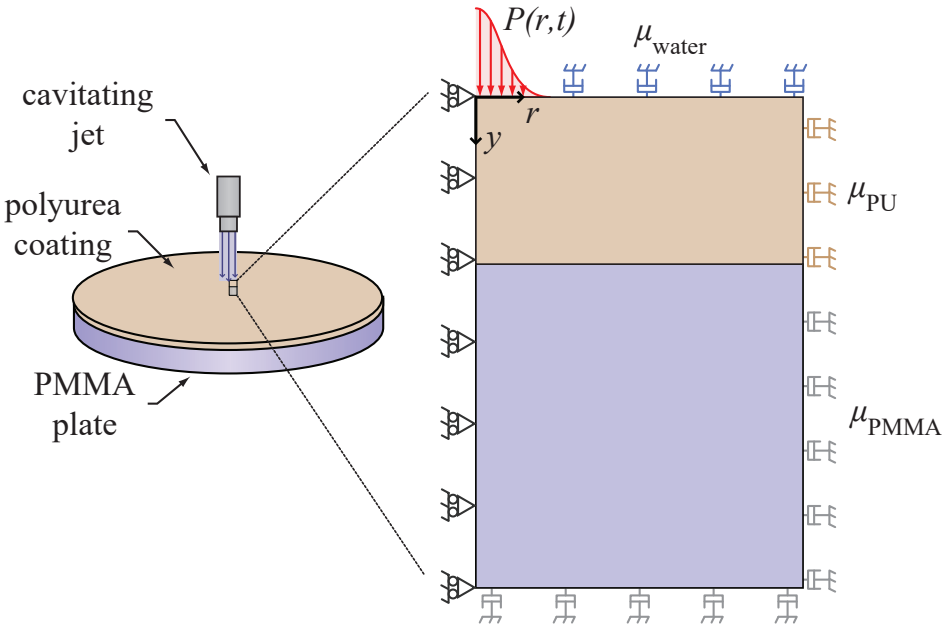

Figure 4.1: Finite element model of coated surface subject to a single bubble impact.

represent the shock pressure, leading to inaccurate input energy. It is unnecessary to refine the mesh around the impact center, because 1), the time step is still limited by the smallest element and 2), the larger elements will lead to a larger artificial energy introduced by the viscous bulk damping which will be discussed later. The timestep is the estimated critical time step according to the CFL condition, multiplies a factor of safety 0.4:

$$\Delta t = 0.4 \times \frac{h_e}{c} \tag{4.1}$$

where h_e is the element length.

A mesh convergence study has been conducted to decide the element length. As shown in Fig. 4.3, the dissipated energy converges along increasing number of elements. Although the energy differences between coarse mesh and fine mesh is small (in the order of 0.01 mJ), the error will be exaggerated after integrating the energy

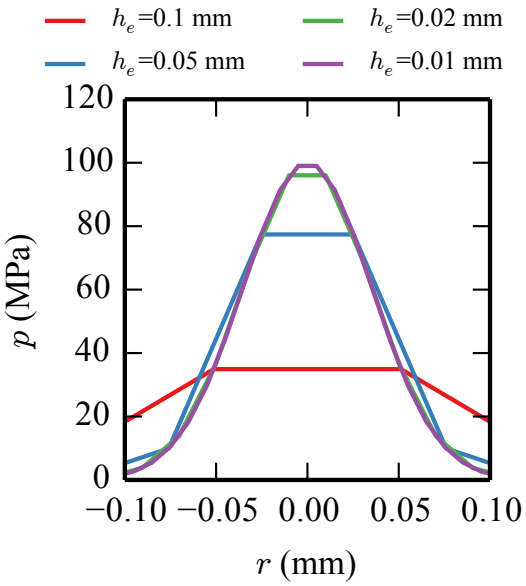

Figure 4.2: The radial discretization of an impulsive load of R_h=0.05 mm by different element sizes

over the bubble distribution. So the relatively fine mesh with 20 μm element length is chosen considering both accuracy and efficiency.

To suppress the wave reflections at the boundary of the simulation domain, a viscous damping boundary condition, denoted by dash pots in Fig. 4.1, is applied at the outer radial and lower boundaries. At these boundaries, a damping traction is calculated to compensate for the momentum flux leaving the prescribed domain,

$$\bar{\mathbf{t}}_d = \mu \mathbf{v}, \quad \text{where} \quad \mu = \rho c \tag{4.2}$$

where ρ and c are the density and wave speed of the material at the boundary respectively and $\mathbf{v}$ is material velocity evaluated at the boundary. As the wave speed varies for shear and longitudinal waves, the boundary traction is decomposed into normal and tangential components, proportional to the normal and tangential components

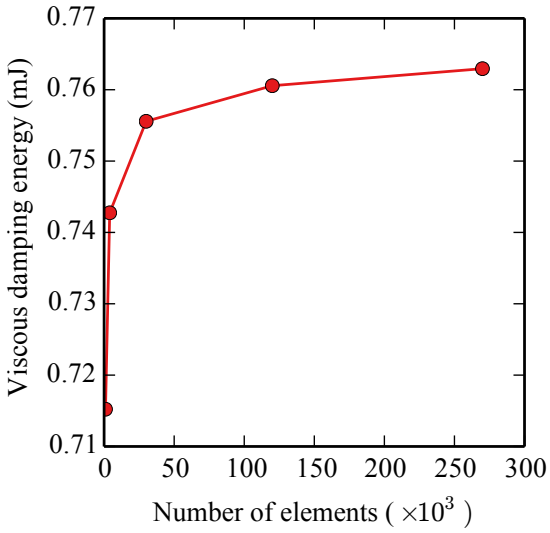

Figure 4.3: Viscous energy dissipation within the coating with different mesh sizes

of velocity field at the boundary:

$$\bar{\mathbf{t}}_d = \bar{\mathbf{t}}_p + \bar{\mathbf{t}}_s = \rho(c_p v_n \boldsymbol{n} + c_s v_t \boldsymbol{t}), \tag{4.3}$$

where c_p and c_s are the longitudinal and shear wave speeds, respectively. Although the wave speeds in polyurea are amplitude and rate dependent, an idealized linear elastic response is used to calculate the boundary tractions as the waves reaching the boundary have significantly decayed amplitude compared to the initial impact stress. Furthermore, as the reflected energy at the polyurea boundary was observed to be minuscule compared to the viscous dissipation, the error in heat generation due to the reflection is insignificant.

The interaction between the fluid and coating surface is crudely approximated by a damping boundary condition matched to the impedance of water. The reduction of the impedance of water due to the presence of a vapor phase is not considered. Furthermore, as water can only transmit a compressive wave, the normal component of the applied viscous traction is restricted to only compressive traction, i.e. if the

surface is moving away from the fluid, the surface traction is zero. The shear traction is also zero, neglecting any shear boundary layer applied by the fluid. These approximations are necessary to allow for the analysis of a cavitating environment where a large number of bubble collapses take place. Fully coupled fluid-structure simulations that more accurately represent the loading dynamics are left to a subsequent publication.

A quadratic bulk viscosity damping is introduced to remove spurious pressure oscillations resulting from the spatial discretization of the finite elements, and to regularize the pressure discontinuity resulting from the impact load across several elements. The bulk viscosity adds a contribution to the pressure in the form

$$p_{ed} = \begin{cases} b_1 \rho c h_e D_v - b_2 \rho (h_e D_v)^2, & D_v < 0 \\ 0, & D_v \geq 0 \end{cases}, \tag{4.4}$$

where D_v is the volumetric deformation rate, $b_1 = 0.06$ and $b_2 = 1.2$ the non-dimensional damping parameters, ρ is the material density, and κ is the bulk modulus. The artificial energy introduced by the damping can be calculated as the damping pressure p_{ed} multiplies the change of the volume ΔV. Then since the pressure is scaled by the element length, the artificial energy in a large element would be larger than the total artificial energy of smaller elements with the same total volume.

4.2 Energy Conservation

Summarizing all components of this model, the energy conservation equation of this model can be expressed as

$$W_{ext} = U + E_k + W_{vd} + W_{bd} + W_{ed} \tag{4.5}$$

where the notations are explained in table 4.1.

W_{ext}	External energy
U	Strain energy
E_k	Kinetic energy
W_{vd}	Viscous damping energy
W_{bd}	Boundary damping energy
W_{ed}	Explicit damping energy

Table 4.1: Notation of different kinds of energies.

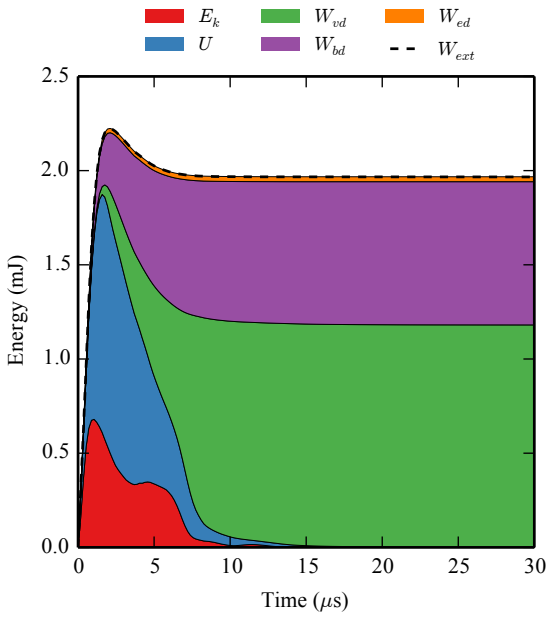

Figure 4.4: Energy history from all sources within PU-650 coating subject to a R_h =500μm and p_m =100 MPa bubble collapse event.

In Fig. 4.4 the history of each kind of energy is plotted as stacked area to show the dynamic energy flow in the material. It is clear that the system has come to a stable state in 20 μs as the energy stops changing. The kinetic energy E_k and strain energy U rises up when the impact happens and goes to zero when the material is relaxed after the load removes. The viscous dissipation energy W_{vd} occupies the largest area at the end indicates that the energy converted into heat is significant. The boundary damping energy W_{bd} forms the second largest area, thus the energy flows into the neighboring regions, the water beyond the top, substrate below the bottom, and adjunct material in the radial direction, that are outside of the simulation domain is also significant. However, only the proportion that damped at the radial boundary of the coating will affect the material heating calculation and it is small compared with the material dissipation. The smallest area is the explicit artificial damping W_{ed}, so the extra energy brought into the system by the bulk viscosity damping is very limited. A dashed representing the overall work done by the external force is plotted on top of the stacked energies and matches with the edge very well. In fact the error of the energy conservation, i.e. $W_{ext} - (U + E_k + W_{vd} + W_{bd} + W_{ed})$, is at the order of 10^{-7} J.

When relating the fluid aggressiveness to the impulsive load in FEM model, linear scaling factors were introduced, namely, the time scaling factor α and the radius scaling factor β. We also investigated the two factors' influence on the energy conversion, including the conversion rate from the bubble's total energy to the work done to the material by the resulting water hammer ($\eta_1 = W_{ext}/E_{total}$) and the conversion rate from mechanical energy to thermal energy within the material ($\eta_2 = W_{vd}/W_{ext}$). As shown in Fig. 4.5, for a fixed bubble collapse load with the peak pressure of 5 MPa and characteristic radius of 0.1 mm, β effects η_1 in a power law with the order of 2.4. This indicates that β strongly affects how much energy actually flows into the

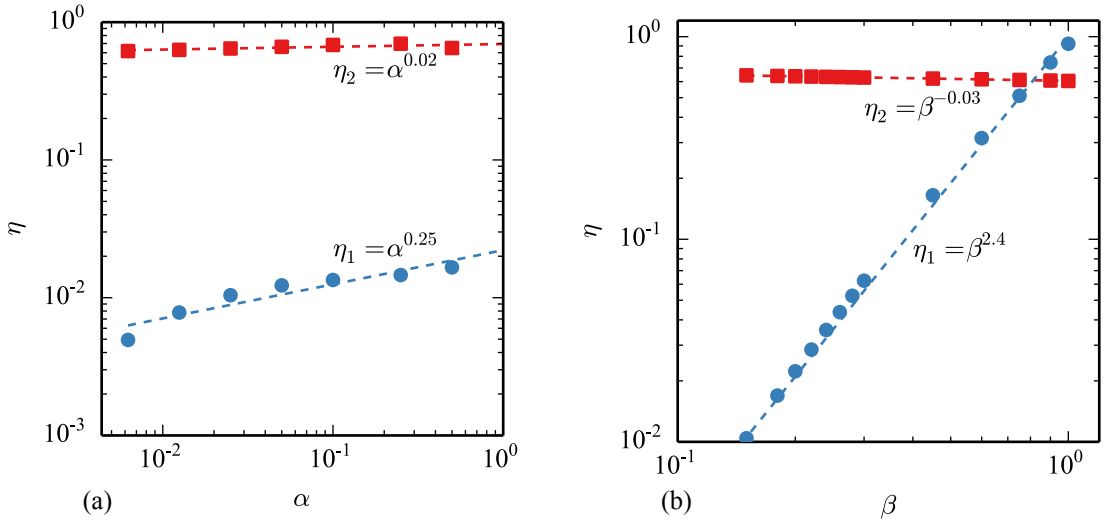

Figure 4.5: Power law correlation between the energy conversion rates (η_1 and η_2) and the scaling factors (a) α and (b) β.

material as the work done by the water hammer. Nevertheless, α does not affect η_1 as significantly as β since the corresponding power function order is only 0.25. The η_2, which represents the proportion of external energy dissipated into heat within the material, does not vary with both of the parameters. Because the material heating is determined by its properties and the load shape while α and β are parameters related to fluid aggressiveness.

4.3 Temperature Measurement

The temperature within the polyurea coating is directly measured during the cavitating jet experiment using thermocouples in the Dynaflow laboratory. As shown in Fig. 4.6, a 2 mm thick polyurea coating adheres to a PMMA sample holder of 4 mm thick below the coating and a cavitating jet is applied at the sample center. The thermocouples are inserted 0.5 mm deep into the sample from the bottom and aligned in the radial direction with 2.54 mm interval distance.

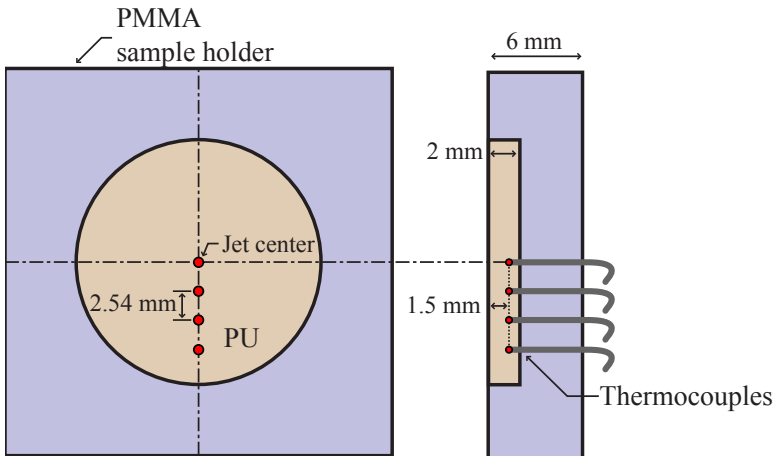

Figure 4.6: The cavitating jet experiment with thermocouple recording the temperature 1.5 mm below the surface.

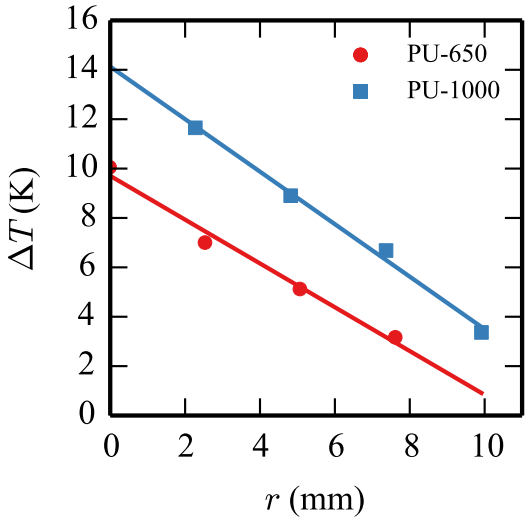

Figure 4.7: Temperature rise in PU-650 and PU-1000 at different radius under 2.75 MPa cavitating jet after 5 minutes.

Then the radial temperature distribution at $y = 1.5$ mm after exposing the sample to 2.75 MPa cavitating jet for 5 minutes is directly measured as shown in Fig. 4.7. From the cavitating jet center to the edge, the temperature rises decays in a linear order. The slopes of the curves, which is the radial temperature gradient dT/dr, are similar for both materials, 0.887 K/mm for PU-650 and 1.063 K/mm for PU-1000. It is also clear that the PU-1000 coating is heated to a higher temperature than the PU-650 coating under the same cavitation loading. Note that although this is a different experiment from the one measuring impulsive pressure pulses introduced in section 2.2, we assume that the cavitation aggressiveness in both experiments are the same since the experiment setups are the same, including the jet pressure, nozzle standoff, and nozzle diameter. Therefore the temperature rise measured here is directly related to the bubble collapse loads recorded in section 2.2.

It is necessary to note that the temperature difference in radial direction causes a certain amount of heat flux from the center to the periphery. We are neglecting this flux in the following heat transfer model because the amount of heat flowing out of the system is small as the heat conductivity of polyurea is small and the temperature gradient at a different depth is not measured. As a consequence, the temperature at thermal steady state will be overestimated in the numerical model.

4.4 Heat Transfer Model

The dissipated energy density along the thickness is integrated over the corresponding cross section. By summing up these energy densities obtained from the sampling FEM simulations corresponding to the conditions shown in Fig. 2.10, a macroscopic heating power - depth curve can be obtained:

$$s(y) = \sum_i A^i \int_0^{2\pi} \int_0^{\infty} f(R_h^i, p_m^i) e_D^i(r, y) r dr d\theta, \tag{4.6}$$

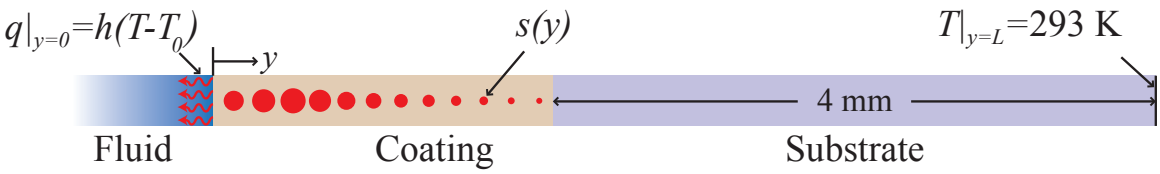

Figure 4.8: Simplified 1D heat transfer model.

where $e_D^i(r, y)$ is the dissipated energy density function at coordinate (r, y) of the i^{th} sampling simulation and $f(R_h^i, p_m^i)$ is the frequency of bubbles detected within the i^{th} sampling region that is near the point (R_h^i, p_m^i). $A^i = \Delta(\log(p_m))\Delta R_h$ is the area of the i^{th} sampling region in the frequency density distribution function.

Then a simplified 1D heat transfer model can be built as illustrated by the schematic in Fig. 4.8. The heat is generated within the coating material and conducted into the substrate, fluid, and the outer layer material in the radial direction. The temperature at the interface is continuous all the time. The heat flux towards the fluid q is linearly related to the temperature difference between water and structure surface by the heat transfer coefficient h. Then the heat equation and the boundary conditions can be written as:

$$\begin{aligned} A_t C\frac{\partial T}{\partial t} &= A_t\kappa\frac{\partial^2 T}{\partial y^2} + s(y), \\ T|_{y=L} &= T_0 \\ \text{and } q|_{y=0} &= h(T|_{y=0} - T_0) \quad , \end{aligned} \tag{4.7}$$

where A_t is the trasducer area. The expression can be rearranged as:

$$C\dot{T} - \kappa\nabla^2 T = \frac{s(y)}{A_y} \tag{4.8}$$

and can be solved by FEM with the weak form:

$$\int_\Omega \delta T C\dot{T} d\Omega = \int_\Omega \nabla\cdot(\delta T\kappa\nabla T) - \nabla(\delta T)\kappa\nabla T d\Omega + \int_\Omega \delta T s(y) d\Omega \tag{4.9}$$

Discretizing the above weak form using 1D shape function N_I, a matrix first order equation is obtained:

$$\begin{aligned}\delta T_I \int_\Omega N_I C N_J d\Omega \dot{T}_J = \delta T_I \left(\int_\Gamma N_I \overline{q} d\Gamma - \int_\Omega B_I k B_J d\Omega T_J \right. \\ \left. + \int_\Omega N_I N_J d\Omega s_J \right) \\ C M_{IJ} \dot{T}_J = F_I - K_{IJ} T_J + M_{IJ} s_J\end{aligned} \tag{4.10}$$

Applying the Crank-Nicolson time update method, we finally get a matrix inverse problem

$$\begin{aligned}\left(C\frac{\boldsymbol{M}}{\Delta t} + \frac{\boldsymbol{K}}{2} \right) \boldsymbol{T}^{n+1} = \left(C\frac{\boldsymbol{M}}{\Delta t} + \frac{\boldsymbol{K}}{2} \right) \boldsymbol{T}^n + \boldsymbol{F} + \boldsymbol{M}\boldsymbol{S} \\ \boldsymbol{A}\boldsymbol{T}^{n+1} = \boldsymbol{B}^n\end{aligned} \tag{4.11}$$

Using the empirical relationship given by Martin [96], the average heat transfer coefficient of the impinging jet was computed to be 220 kW/(m^2·K), however we note that for a heat transfer coefficient greater than 50 kW/(m^2·K), the temperature at the surface of the coating remains the same as the water temperature, effectively imposing a Dirichlet boundary condition.

The purpose of building this heat transition model is to predict the temperature rise of the system and compare the temperature rise of different thicknesses. It is also a method to validate the statistic model by comparing the temperature with the thermocouple records in the cavitating jet experiment. Necessary assumptions have been made for this model: 1, the heat is linearly accumulated from each bubble without considering the consecutiveness of bubble impacts; 2, the material is always heated up from environment temperature T_0 for each bubble impact; 3, the structural deformation dynamics is not considered in the 1D heat transfer model.

Table 4.2 summarizes the material constants of the heat transfer model.

To summarize this chapter, the FEM simulations are built according to the hydrodynamic loads distribution and proper boundary conditions are built to mimic the real

Parameter	PU650	PU1000	PMMA
κ (W/(m·K)):	0.20	0.20	0.19
C (J/(cm^3·K)):	1.98	1.98	1.61
ρ (g/cm^3):	1.13	1.09	1.19

Table 4.2: Material parameters used in the constitutive model according to [97, 98]

stress wave propagation dynamics. The heat generation is predicted by the thermo-mechanical viscoelastic material model. As a bridge between single impact heating and macroscopic heating resulted from massive bubble impacts, a one-dimensional heat transfer model is solved and the total heating power of polyurea coating can be computed.

Chapter 5

ANALYSIS OF HEATING AND DEFORMATION IN POLYUREA COATINGS

5.1 Material Deformation Under Bubble Collapse Load

The FEM simulations provide an insight into the dynamic response of polyurea coatings under bubble collapse loads. From the simulations, we can visualize the material deformation subjected to a bubble collapse impact. It is also of importance to tell the bounds of strain and strain rate within the material in order to help in designing experiments and optimizing materials. To characterize the range of magnitudes and strain rates encountered by the coating under a collapse pressure, we examine the deformation resulting from two representative bubble collapse loads, one with hydrodynamic loading radius $R_h = 0.05$ mm and the other with $R_h = 0.5$ mm. The pressure amplitudes of the two loads are set to be equal that $p_m = 100$ MPa. The load durations are calculated according to Eq. (2.8): $\tau = 0.22$ μs for the smaller load and $\tau = 2.26$ μs for larger load.

Fig. 5.1 and Fig. 5.2 show the equivalent strain ($\epsilon_{eq} = \sqrt{\frac{2}{3}\boldsymbol{\epsilon}' : \boldsymbol{\epsilon}'}$) wave and vertical normal strain ϵ_{yy} waves (p wave) respectively. It is obvious that both of the maximum equivalent strain and maximum axial strain happen at the upper part of the coating. The deformation reaches the peak at around $t = 0.5\tau$ and is mostly damped at $t = 1.5\tau$. Tension axial wave (positive ϵ_{yy}) is also observed near the surface, because while the compression load pushes the material down along the central line, the material at the periphery of the sinking surface is being pushed out of the pit and tensile stress is generated below. For polyurea, the tensile stress will build damage

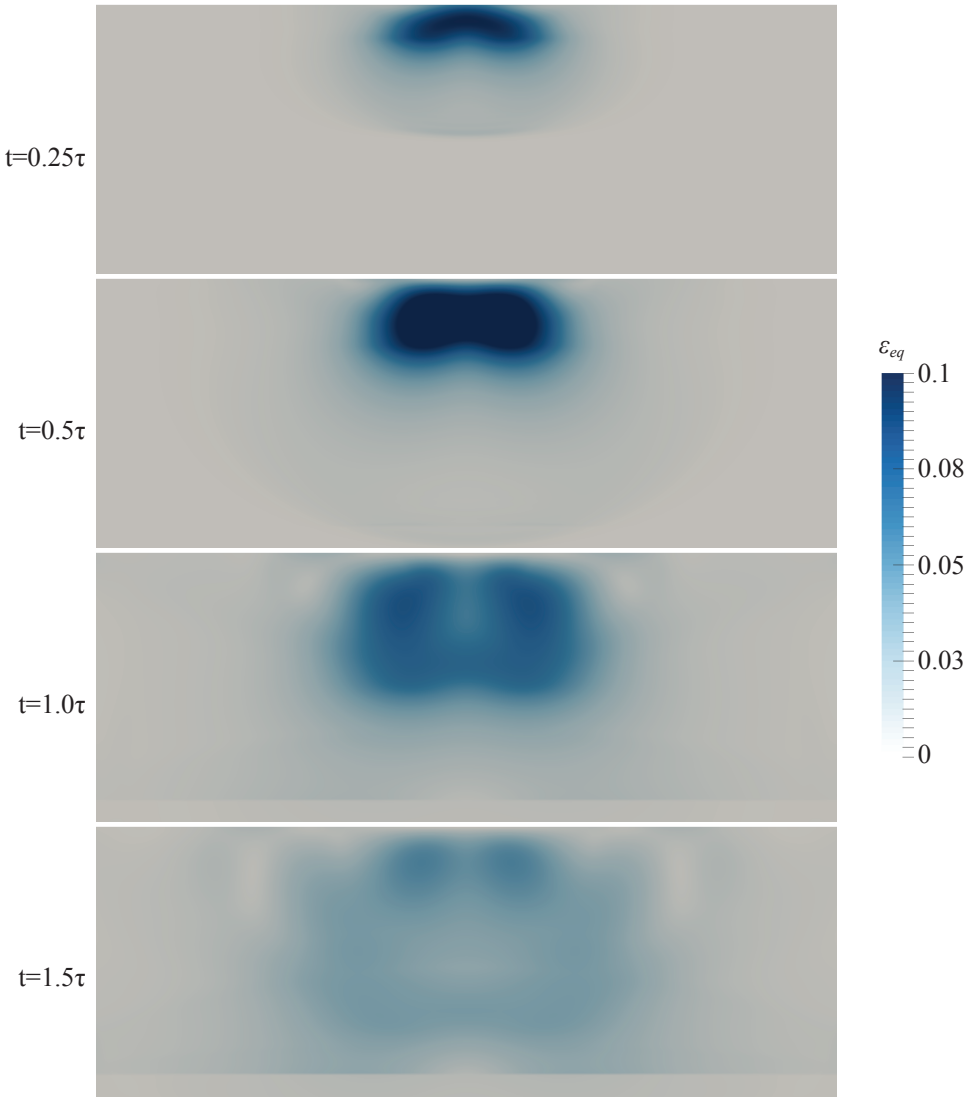

Figure 5.1: The equivalent strain wave propagating through the PU-650 coating under $R_h = 0.5$ mm impulsive load.

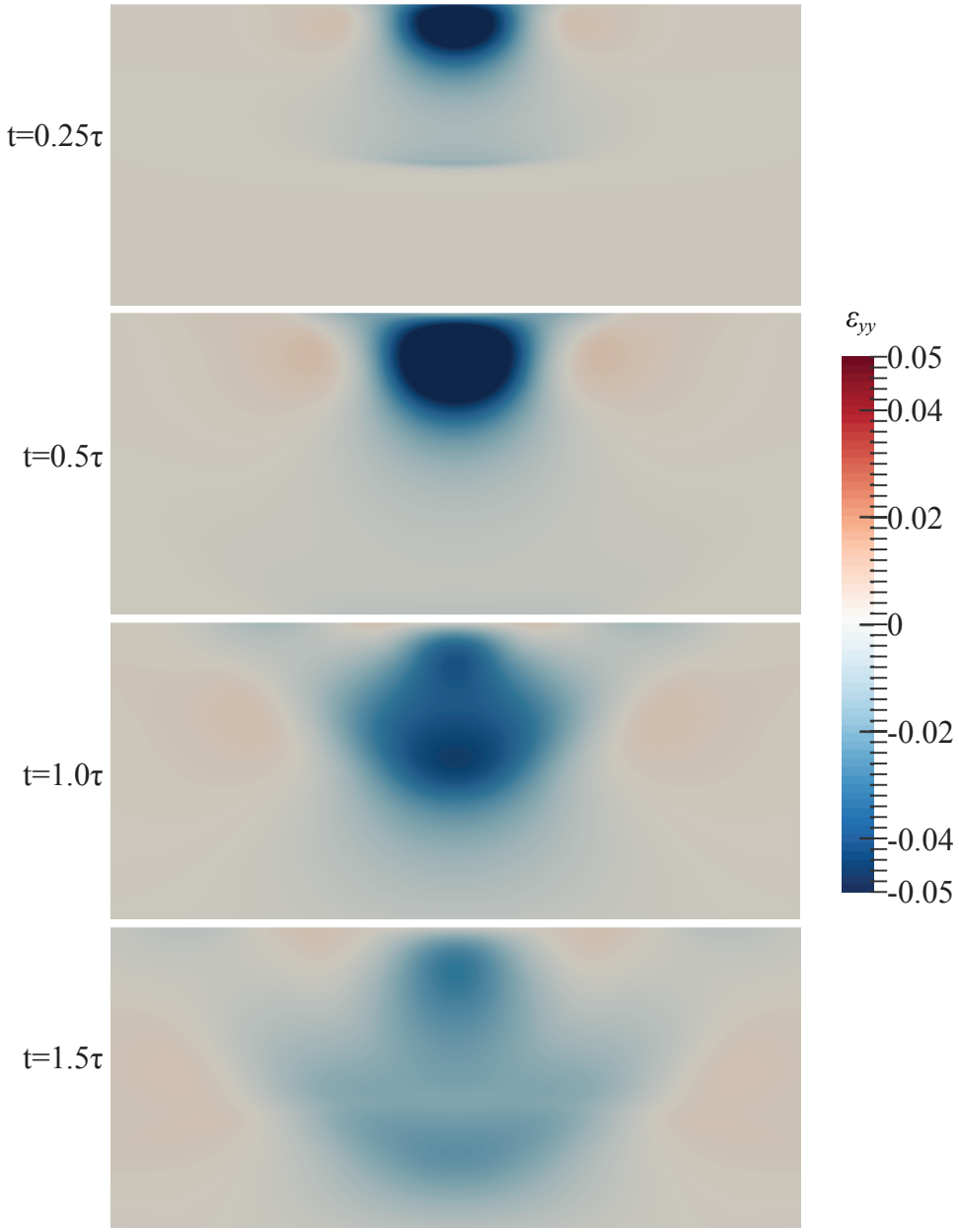

Figure 5.2: The Y axial strain wave propagating through the PU-650 coating under $R_h = 0.5$ mm impulsive load.

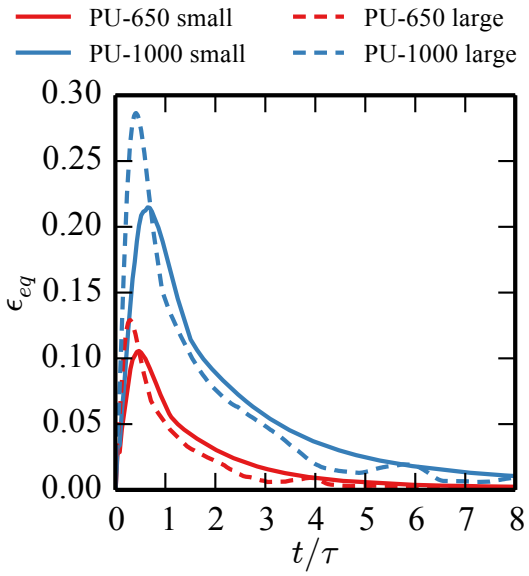

Figure 5.3: Maximum equivalent strain history during a large bubble and a small bubble impact with time axis normalized by loading duration τ.

more quickly than compression because its tension stiffness is much weaker than the compression stiffness.

Fig. 5.3 shows the history of equivalent strain ($\epsilon_{eq} = \sqrt{\frac{2}{3}\boldsymbol{\epsilon}' : \boldsymbol{\epsilon}'}$) in a 2 mm thick polyurea coating under the two representative impulsive loadings. The equivalent strain histories were recorded at the locations of maximum deviatoric stress (at depths of approximately 5 μm and 150 μm below the surface for the small and large bubbles, respectively) and show a similar trend for different bubble sizes and materials when scaled by the load duration. However, PU-1000 has a significantly higher strain amplitude than PU-650, reaching 30% under the large bubble.

With regard to the strain rates, the smaller bubble collapse load generates larger shear strain rate (1.7×10^6 s^{-1} for PU-650 and 2.6×10^6 s^{-1} for PU-1000) as compared with the larger loads (1.3×10^6 s^{-1} for PU-650 and 1.5×10^6 s^{-1} for PU-1000).

In a single bubble simulation, minor energy is dissipated within the material. As

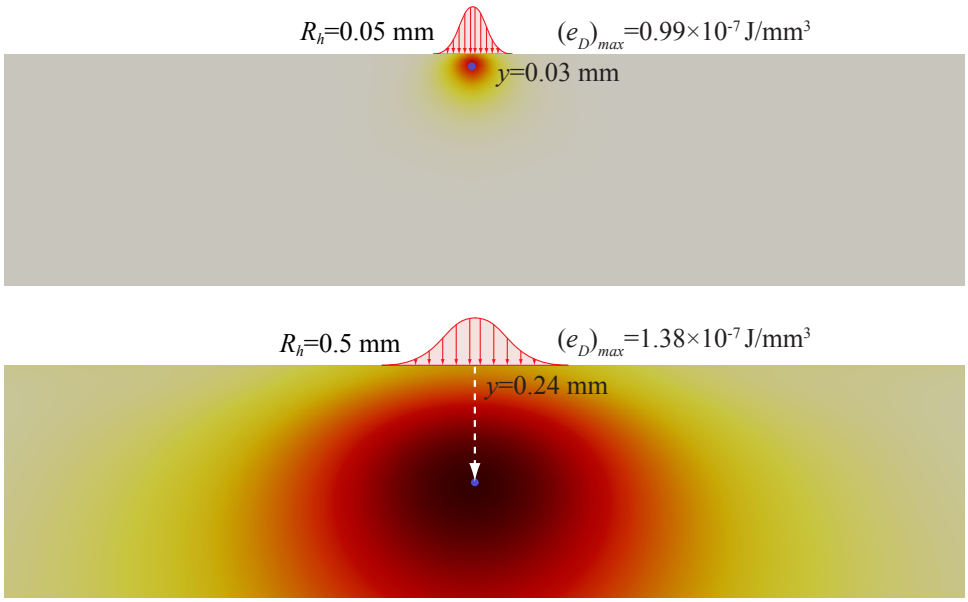

Figure 5.4: PU-650 coating heat map under single bubble collapse loads with different radius.

shown in Fig. 5.4, the heating energy density is as small as in an order of 10^{-7} J/m^3 and maximum temperature change is up to 0.27 K. The location of the heating hot spot is related to the characteristic radius. Although the hot spots from two pressure loads are at different depth, they both appear at the center line where $r = 0$. Thus the maximum energy dissipation always happens vertically below the center of the load.

5.2 Thermal Energy Distribution

With FEM simulations, we have a clear understanding of the energy conversion during a single bubble collapse event. According to Rayleigh model, the total energy E_{total} that a single bubble possesses can be estimated as the collapsing pressure times the bubble volume. When the bubble collapses, a portion of the total energy is converted to the external work done to the coating, denoted as W_{ex}. Then the energy

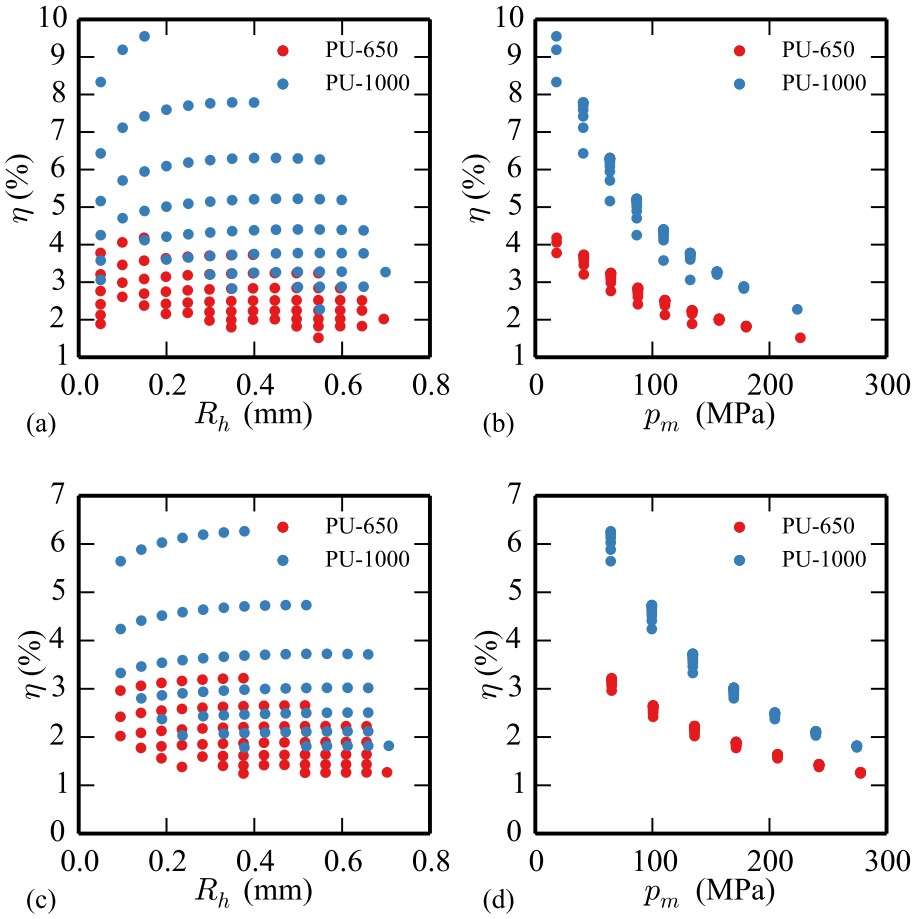

Figure 5.5: The percentage of maximum bubble potential energy converted to force work done to the material with different load radius and peak pressure.

conversion rates $\eta = W_{ex}/E_{total}$ can be an effective measurement of the cavitating efficiency. As shown in Fig. 5.5, the conversion rates of different bubbles are marked in R_h and p_m coordinates. The conversion rate is mostly independent of the load radius R_h but highly influenced by the maximum pressure p_m.

For a single bubble simulation, the energy dissipated within the material under the larger and more powerful bubble is higher than the smaller bubble. However, considering the frequency density of the bubble impacts, it is not the larger bubbles

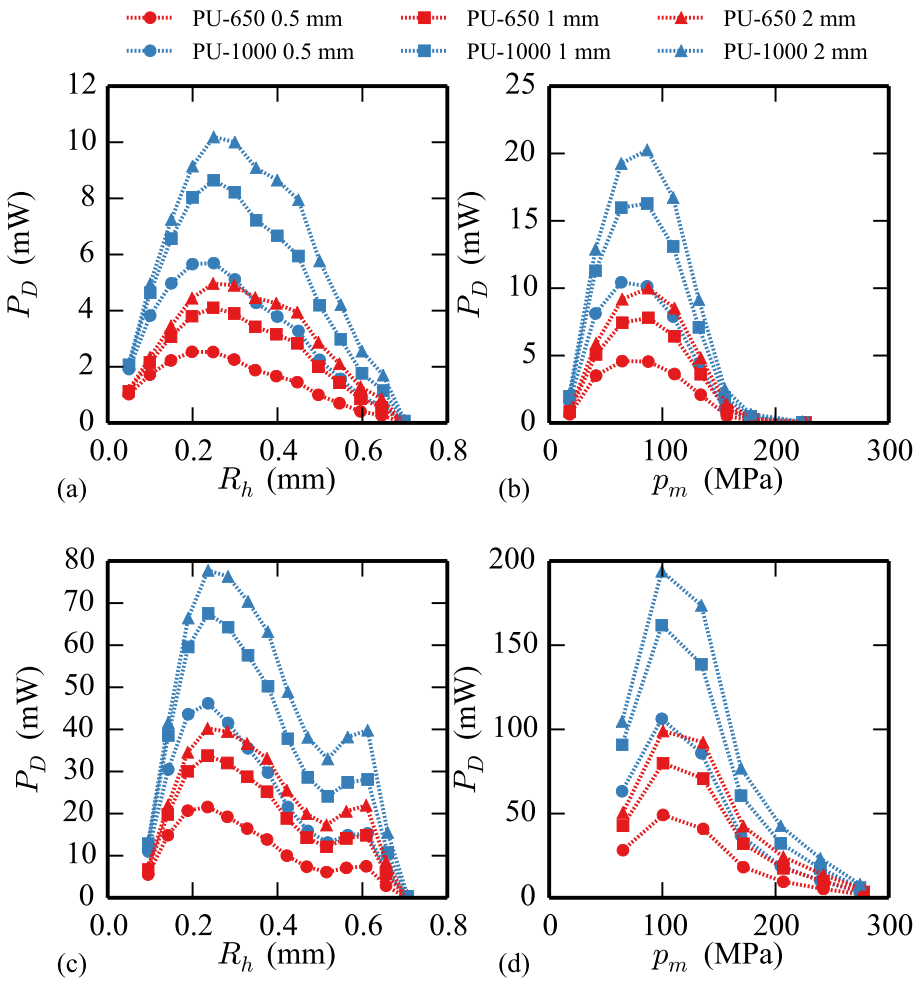

Figure 5.6: Integrated heating power contributed by bubble collapse loads with different radius R_h and peak pressure p_m under 2.75 MPa (a)(b) and 5.52 MPa (c)(d) cavitating jet pressure.

making the major contribution to the material heating. Because as suggested by Fig. 2.11, the frequency of the loads decreases rapidly as the radius and maximum pressure increases. As shown in Fig. 5.6, considering both energy and frequency factors, the loading radius at 0.25 mm generate the most heating power for both materials. The most harmful pressure amplitude shifts under higher cavitating jet pressure: around 80 MPa under 2.75 MPa jet pressure and 100 MPa under 5.52 MPa jet pressure.

It is also shown in Fig. 5.6 that thicker coatings generate higher heating power than thinner coatings. This result agrees with the experimental observations that a thinner coating is more resist to cavitating jet than a thicker coating. In the cavitating experiment, under the same cavitation conditions, the 1 mm coating showed little or none damage while 3 mm and 9 mm coating presented significant local melting and failure. Even comparing the two thicker coatings, the 3 mm coating failed later than 9 mm coating under the cavitating jet.

5.3 Temperature Distribution Through Coating Thickness

It is also of high interest to study the heating power along the coating thickness to find the most heated location. As shown in Fig. 5.7(a)(c), the location of the maximum heating power density is always at a depth of 0.15 mm below the surface regardless of the coating thickness, material, or flow condition. With a lower molecular weight, PU-650 dissipates less energy than PU-1000 under the same cavitating environment. Under a higher cavitating jet pressure, the maximum heating power density increases drastically (7 times) for both materials. In a future work, it is of high interest to find the factor that determines the peak power density location.

It is also noticeable that the heating power rises at the interface between the coating and the substrate. This is due to the discontinuity in material impedance

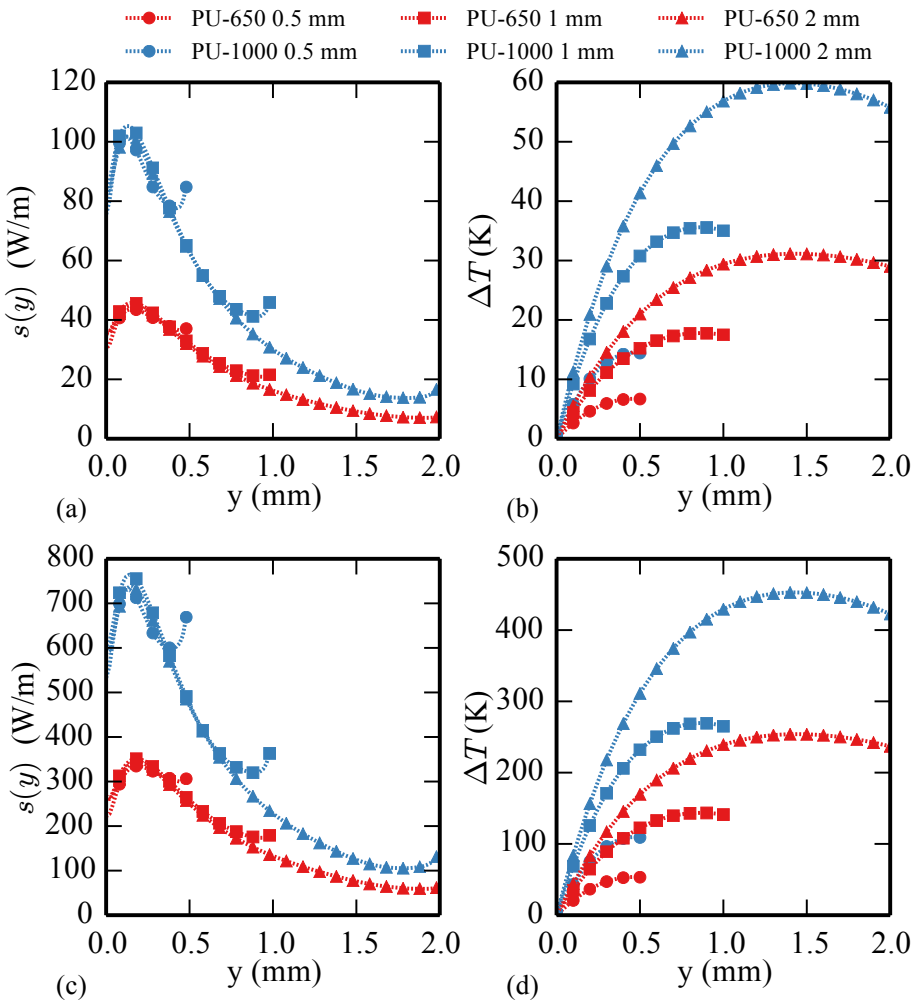

Figure 5.7: Under 2.75 MPa (top) and 5.52 MPa (bottom) jet pressure, material heating power distributions are shown in (a)(c) and temperature rise in (b)(d).

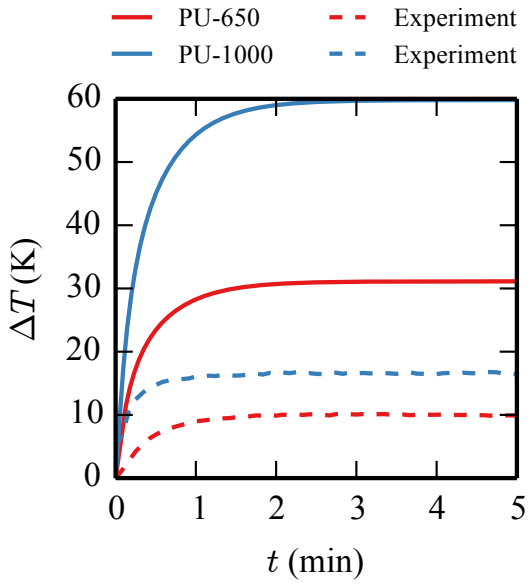

Figure 5.8: Temperature history of 1.5 mm below surface within a 2 mm coating under 2.75 MPa cavitating jet.

at the interface that leads to a difference in radial wave speed and therefore induces significant shear stress and dissipation within the polyurea coating.

Solving the heat equation 4.7 for 5 min with Crank-Nicolson implicit time integrator, a steady state temperature distribution is obtained. To validate the numerical model, the temperature rise of 2 mm coatings with two materials are compared with the data recorded by the temperature measurement experiment. The PU-650 coating has been heated up 10 K at the cavitating jet center during the experiment.

The steady state temperature distribution along the thickness is plotted on the right column in Fig. 5.7. It shows that the thicker coating is heated to a higher temperature than thinner coating under same loading condition. Therefore, the thicker coating is less resistant to cavitation erosion as the material melts faster. The cause is currently concluded as 1, total amount of heat within thinner coating is less than

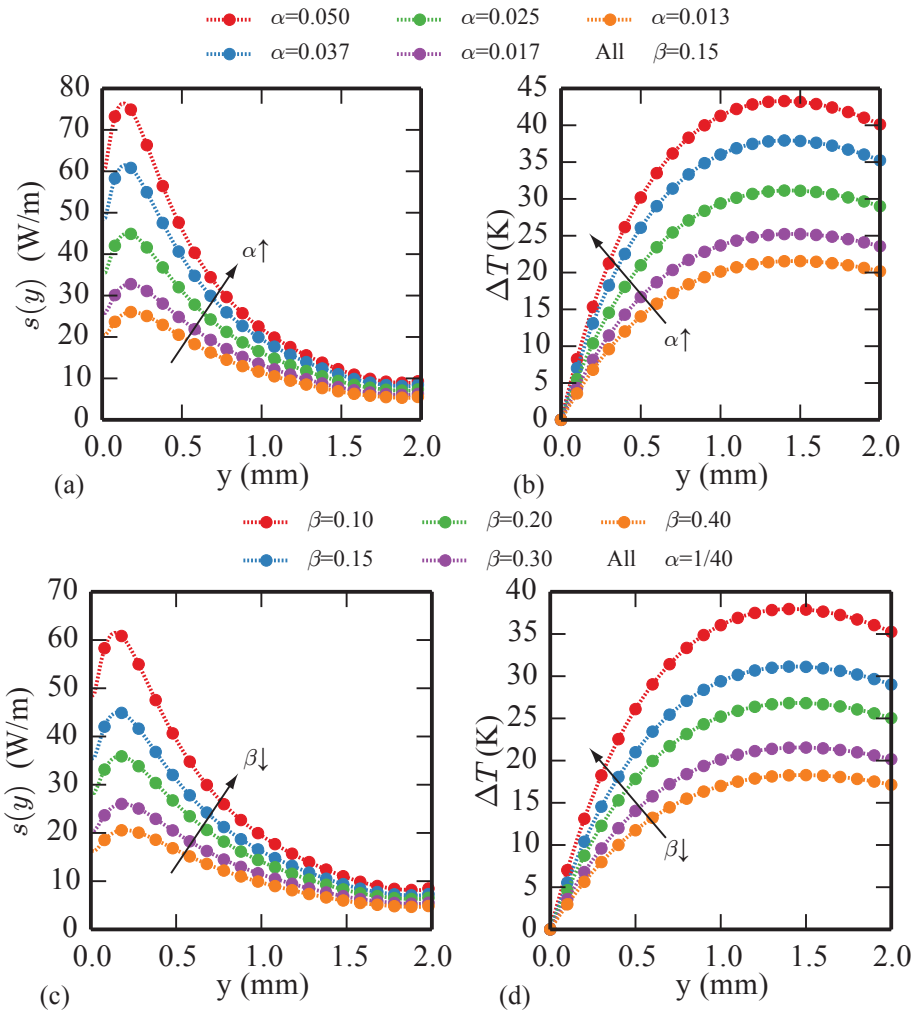

Figure 5.9: The different predictions of heating power and temperature rise for 2 mm PU-650 coating under 2.75 MPa cavitating jet by using different α and β.

thicker coating because of less mass; 2, the heating hot spot for thinner coating is closer to the substrate interface and the fluid, therefore the overall heat transfer efficiency is higher.

Fig. 5.8 shows the temperature history at $y = 1.5$ mm predicted by our numerical model compared with the experimental data. One direct reason for overpredicting the temperature is that no radial thermal conduction is considered in this model as

discussed in section 4.3. Another potential cause is that the temperature prediction is sensitive to the scaling factors used to correlate the surface impulsive pressures with experimental measurements, such as factor α and β. Although these scaling laws are derived from hydrodynamic principals, linearization and average approximation are adopted in the process that would bring errors. As shown in Fig. 5.9, the $s(y)$ and ΔT distribution along y can be shifted down by using a smaller α and larger β value. It is not complicated to further fit the two parameters if sufficient experimental data is given, but that is not conducted in this work since we emphasize the model's capability of coupling both fluid aggressiveness and material impedance to analyze the elastomer failure. Additionally, a conjectural error resource is that under the high amplitude impact shock loads, the material reaches a high strain (up to 30% as discussed in section 5.1) where the viscoelastic model with linear elasticity is not accurate anymore. In this case, to combine a nonlinear elastic model, e.g., a hyperelastic law, is needed to eliminate the error for large deformation.

Chapter 6

SUMMARY

We have investigated the heat generation in elastomeric coatings subjected to cavitating flows through a combined experimental and modeling effort, in which measured cavitation pressure pulses were approximated by a parameterized surface load model. Although the model does not explicitly incorporate the complete hydrodynamic details governing the distribution of pressure exerted on a surface due to each bubble collapse, e.g., collective collapse from multiple bubbles, shock driven collapse, the standoff distance of collapsing bubbles, or non-spherical bubble collapse, these effects are implicitly embedded within the calculated distribution of *representative* bubble collapses.

The elastomeric coatings were modeled by a viscoelastic model incorporating the effects of temperature and pressure on the stress relaxation spectrum. The kinematics of the model in large deformation has been extensively discussed and the reason for choosing logarithmic formulation has been explained. Additionally, an enriched model coupled with hyperelasticity and plasticity has been presented and preliminary results have been shown. However, the lack of experimental data limits this work to a prospective demonstration of the logarithmic formulation framework for building more comprehensive constitutive models for elastomers.

The analysis of the cumulative effect of a distribution of single bubble impacts, reveals that the amount of heating due to the viscoelastic dissipation of impact loads results in a significant temperature rise of the polyurea coating. As the mechanical properties of elastomers are quite sensitive to temperature this high rate of heating implies a critical failure mechanism: as the temperature increases both relaxation

times and the yield strength decrease, leading to accelerated inelastic deformation and runaway heating.

The innovation and contribution of this work can be summarized 1) a direct correlation between pressure transducer records in cavitating jet experiment to microscopic hydrodynamic pressure load parameters is established according to bubble dynamics and CFD simulations; 2) a logarithmic co-rotational rate form constitutive model for polyurea including viscous heating is built based on the prior work by Amirkhizi; 3) a numerical framework that converting FEM simulation results for single impact heating to macroscopic material heating is constructed.

As an extension of this work, we will attempt to quantitatively model this potential failure mechanism by coupling the mechanical and thermal models. Further efforts are needed to more accurately model the material response under more intense cavitating flows where nonlinear material effects play a larger role. However, the parameterization of more complex material models remains a significant challenge at the extreme loading rates and pressures generated in cavitating flows.

REFERENCES

[1] L Rayleigh. On the pressure developed in a liquid during the collapse of a spherical cavity. *The London, Edinburgh, and Dublin Philosophical Magazine and Journal of Science*, 34(200):94–98, 1917.

[2] C F Naude and A T Ellis. On the mechanism of cavitation damage by nonhemispherical cavities collapsing in contact with a solid boundary. *Journal of Fluids Engineering*, 83(4):648–656, 1961.

[3] R Hickling and M S Plesset. Collapse and rebound of a spherical bubble in water. *Physics of Fluids (1958-1988)*, 7(1):7–14, 1964.

[4] T B Benjamin and A T Ellis. The collapse of cavitation bubbles and the pressures thereby produced against solid boundaries. *Philosophical Transactions of the Royal Society of London A: Mathematical, Physical and Engineering Sciences*, 260(1110):221–240, 1966.

[5] M S Plesset and R B Chapman. Collapse of an initially spherical vapour cavity in the neighbourhood of a solid boundary. *Journal of Fluid Mechanics*, 47(02):283–290, 1971.

[6] J R Blake and D C Gibson. Cavitation bubbles near boundaries. *Annual Review of Fluid Mechanics*, 19(1):99–123, 1987.

[7] GL García, V López-Ríos, A Espinosa, J Abenojar, F Velasco, and A Toro. Cavitation resistance of epoxy-based multilayer coatings: Surface damage and crack growth kinetics during the incubation stage. *Wear*, 316(1):124–132, 2014.

[8] T Deplancke, O Lame, JY Cavaille, M Fivel, M Riondet, and JP Franc. Outstanding cavitation erosion resistance of ultra high molecular weight polyethylene (uhmwpe) coatings. *Wear*, 328:301–308, 2015.

[9] S Chi, J Park, and M Shon. Study on cavitation erosion resistance and surface topologies of various coating materials used in shipbuilding industry. *Journal of Industrial and Engineering Chemistry*, 26:384–389, 2015.

[10] A Karimi and JL Martin. Cavitation erosion of materials. *International Metals Reviews*, 31(1):1–26, 1986.

[11] RH Richman and WP McNaughton. Correlation of cavitation erosion behavior with mechanical properties of metals. *Wear*, 140(1):63–82, 1990.

[12] H Kato, A Konno, M Maeda, and H Yamaguchi. Possibility of quantitative prediction of cavitation erosion without model test. *Journal of fluids engineering*, 118(3):582–588, 1996.

[13] FT Cheng, P Shi, and HC Man. Correlation of cavitation erosion resistance with indentation-derived properties for a niti alloy. *Scripta Materialia*, 45(9):1083–1089, 2001.

[14] N Berchiche, JP Franc, and JM Michel. A cavitation erosion model for ductile materials. *Journal of fluids engineering*, 124(3):601–606, 2002.

[15] M Dular, B Stoffel, and B Širok. Development of a cavitation erosion model. *Wear*, 261(5):642–655, 2006.

[16] S Hattori and T Itoh. Cavitation erosion resistance of plastics. *Wear*, 271(7):1103–1108, 2011.

[17] Y Tomita and A Shima. Mechanisms of impulsive pressure generation and damage pit formation by bubble collapse. *Journal of Fluid Mechanics*, 169:535–564, 1986.

[18] T Okada, Y Iwai, S Hattori, and N Tanimura. Relation between impact load and the damage produced by cavitation bubble collapse. *Wear*, 184(2):231–239, 1995.

[19] T Momma and A Lichtarowicz. A study of pressures and erosion produced by collapsing cavitation. *Wear*, 186:425–436, 1995.

[20] H Soyama, A Lichtarowicz, T Momma, and E J Williams. A new calibration method for dynamically loaded transducers and its application to cavitation impact measurement. *Journal of Fluids Engineering*, 120(4):712–718, 1998.

[21] J-P Franc, M Riondet, A Karimi, and G L Chahine. Impact load measurements in an erosive cavitating flow. *Journal of Fluids Engineering*, 133(12):121301, 2011.

[22] D Veysset, AJ Hsieh, S Kooi, AA Maznev, KA Masser, and KA Nelson. Dynamics of supersonic microparticle impact on elastomers revealed by real–time multi–frame imaging. *Scientific reports*, 6, 2016.

[23] K-H Kim, G L Chahine, J-P Franc, and A Karimi. *Advanced Experimental and Numerical Techniques for Cavitation Erosion Prediction*. Springer, 2014.

[24] JA Pathak, JN Twigg, KE Nugent, DL Ho, EK Lin, PH Mott, CG Robertson, MK Vukmir, TH Epps Iii, and CM Roland. Structure evolution in a polyurea segmented block copolymer because of mechanical deformation. *Macromolecules*, 41(20):7543–7548, 2008.

[25] SA Tekalur, A Shukla, and K Shivakumar. Blast resistance of polyurea based layered composite materials. *Composite Structures*, 84(3):271–281, 2008.

[26] CM Roland, D Fragiadakis, RM Gamache, and R Casalini. Factors influencing the ballistic impact resistance of elastomer-coated metal substrates. *Philosophical Magazine*, 93(5):468–477, 2013.

[27] RB Bogoslovov, CM Roland, and RM Gamache. Impact-induced glass transition in elastomeric coatings. *Applied physics letters*, 90(22):221910–221910, 2007.

[28] CM Roland and CB Giller. Impact-resistant elastomeric coatings. In RGeorge Barsoum, editor, *Elastomeric Polymers with High Rate Sensitivity: Applications in Blast, Shockwave, and Penetration Mechanics*. William Andrew, 2015.

[29] MR Amini, J Isaacs, and S Nemat-Nasser. Investigation of effect of polyurea on response of steel plates to impulsive loads in direct pressure-pulse experiments. *Mechanics of Materials*, 42(6):628–639, 2010.

[30] S Singh, JK Choi, and GL Chahine. Characterization of cavitation fields from measured pressure signals of cavitating jets and ultrasonic horns. *Journal of Fluids Engineering*, 135(9):091302, 2013.

[31] Song B and Chen W. One-dimensional dynamic compressive behavior of EPDM rubber. *Journal of engineering materials and technology*, 125(3):294–301, 2003.

[32] Song B and Chen W. Dynamic compressive behavior of EPDM rubber under nearly uniaxial strain conditions. *Journal of engineering materials and technology*, 126(2):213–217, 2004.

[33] Nemat-Nasser S. Experimental characterization of polyurea with constitutive modeling and simulation. In *Proceedings of ONR, ERC, ACTD Workshop, MIT, Cambridge, Massachusetts*, 2004.

[34] Yi J, Boyce MC, Lee GF, and Balizer E. Large deformation rate-dependent stress–strain behavior of polyurea and polyurethanes. *Polymer*, 47(1):319–329, 2006.

[35] Jiao T, Clifton RJ, and Grunschel SE. High strain rate response of an elastomer. In *AIP Conference Proceedings*, volume 845, page 809, 2006.

[36] Jiao T, Clifton RJ, and Grunschel SE. Pressure-sensitivity and constitutive modeling of an elastomer at high strain rates. In *AIP Conference Proceedings*, volume 1195, page 1229, 2009.

[37] T Jiao and R J Clifton. Measurement of the response of an elastomer at pressures up to 9 GPa and shear-rates of 10^5–$10^6 s^{-1}$. In *Journal of Physics: Conference Series*, volume 500, page 112036. IOP Publishing, 2014.

[38] Youssef G. *Dynamic properties of polyurea*. 2011.

[39] Roshdy George S Barsoum, editor. *Elastomeric Polymers with High Rate Sensitivity: Applications in Blast, Shockwave, and Penetration Mechanics*. William Andrew Publishing, Oxford, 2015.

[40] El Sayed T, Mota A, Fraternali F, and Ortiz M. A variational constitutive model for soft biological tissues. *Journal of biomechanics*, 41(7):1458–1466, 2008.

[41] El Sayed T, Mock Jr W, Mota A, Fraternali F, and Ortiz M. Computational assessment of ballistic impact on a high strength structural steel/polyurea composite plate. *Computational Mechanics*, 43(4):525–534, 2009.

[42] Li C and Lua J. A hyper-viscoelastic constitutive model for polyurea. *Materials letters*, 63(11):877–880, 2009.

[43] Shim J and Mohr D. Rate dependent finite strain constitutive model of polyurea. *International Journal of Plasticity*, 27(6):868–886, 2011.

[44] Gamonpilas C and McCuiston R. A non-linear viscoelastic material constitutive model for polyurea. *Polymer*, 53(17):3655–3658, 2012.

[45] Amirkhizi AV, Isaacs J, McGee J, and Nemat-Nasser S. An experimentally-based viscoelastic constitutive model for polyurea, including pressure and temperature effects. *Philosophical magazine*, 86(36):5847–5866, 2006.

[46] Mica Grujicic, WC Bell, B Pandurangan, and T He. Blast-wave impact-mitigation capability of polyurea when used as helmet suspension-pad material. *Materials & Design*, 31(9):4050–4065, 2010.

[47] Tong Hui and Caglar Oskay. Computational modeling of polyurea-coated composites subjected to blast loads. *Journal of Composite Materials*, page 0021998311430160, 2012.

[48] Casey J and Naghdi PM. A remark on the use of the decomposition $F = F_e F_p$ in plasticity. *Journal of Applied Mechanics*, 47(3):672–675, 1980.

[49] Nemat-Nasser S. Decomposition of strain measures and their rates in finite deformation elastoplasticity. *International Journal of Solids and Structures*, 15(2):155–166, 1979.

[50] Lee EH. Some comments on elastic-plastic analysis. *International Journal of Solids and Structures*, 17(9):859–872, 1981.

[51] Lee EH. Elastic-plastic deformation at finite strains. *Journal of Applied Mechanics*, 36(1):1–6, 1969.

[52] Naghdi PM. A critical review of the state of finite plasticity. *Zeitschrift für angewandte Mathematik und Physik ZAMP*, 41(3):315–394, 1990.

[53] Baažant ZP. Finite strain generalization of smallstrain constitutive relations for any finite strain tensor and additive volumetric-deviatoric split. *International Journal of Solids and Structures*, 33(20):2887–2897, 1996.

[54] Xiao H, Bruhns OT, and Meyers A. Logarithmic strain, logarithmic spin and logarithmic rate. *Acta Mechanica*, 124(1-4):89–105, 1997.

[55] Xiao H, Bruhns OT, and Meyers A. On objective corotational rates and their defining spin tensors. *International journal of solids and structures*, 35(30):4001–4014, 1998.

[56] Xiao H, Bruhns OT, and Meyers A. Objective stress rates, path-dependence properties and non-integrability problems. *Acta mechanica*, 176(3-4):135–151, 2005.

[57] Xiao H, Bruhns OT, and Meyers A. Elastoplasticity beyond small deformations. *Acta Mechanica*, 182(1-2):31–111, 2006.

[58] Simo JC and Pister KS. Remarks on rate constitutive equations for finite deformation problems: computational implications. *Computer Methods in Applied Mechanics and Engineering*, 46(2):201–215, 1984.

[59] Arruda EM and Boyce MC. A three-dimensional constitutive model for the large stretch behavior of rubber elastic materials. *Journal of the Mechanics and Physics of Solids*, 41(2):389–412, 1993.

[60] G L Chahine, Franc J P, and Karimi A. Cavitation and cavitation erosion. In K-H Kim, G L Chahine, J-P Franc, and A Karimi, editors, *Advanced Experimental and Numerical Techniques for Cavitation Erosion Prediction*, pages 3–20. Springer, 2014.

[61] A Jayaprakash, C-T Hsiao, and G L Chahine. Numerical and experimental study of the interaction of a spark-generated bubble and a vertical wall. *Journal of Fluids Engineering*, 134(3):031301, 2012.

[62] Jin-Keun Choi and Georges L Chahine. Experimental and numerical study of cavitation erosion resistance of a polyurea coating layer. In *Fourth International Symposium on Marine Propulsors, Austin, Texas*, 2015.

[63] G L Chahine, C-T Hsiao, and R Raju. Scaling of cavitation bubble cloud dynamics on propellers. In K-H Kim, G L Chahine, J-P Franc, and A Karimi, editors, *Advanced Experimental and Numerical Techniques for Cavitation Erosion Prediction*, pages 345–372. Springer, 2014.

[64] GL Chahine and KM Kalumuck. Bem software for free surface flow simulation including fluid–structure interaction effects. *International Journal of Computer Applications in Technology*, 11(3-5):177–198, 1998.

[65] KM Kalumuck, R Duraiswami, and GL Chahine. Bubble dynamics fluid-structure interaction simulation by coupling fluid bem and structural fem codes. *Journal of Fluids and Structures*, 9(8):861–883, 1995.

[66] Andrew B Wardlaw Jr and J Alan Luton. Fluid-structure interaction mechanisms for close-in explosions. *Shock and Vibration*, 7(5):265–275, 2000.

[67] G L Chahine. Modeling of cavitation dynamics and interaction with material. In K-H Kim, G L Chahine, J-P Franc, and A Karimi, editors, *Advanced Experimental and Numerical Techniques for Cavitation Erosion Prediction*, pages 123–161. Springer, 2014.

[68] G L Chahine, J-P Franc, and A Karimi. Laboratory testing methods of cavitation erosion. In K-H Kim, G L Chahine, J-P Franc, and A Karimi, editors, *Advanced Experimental and Numerical Techniques for Cavitation Erosion Prediction*, pages 21–35. Springer Netherlands, 2014.

[69] FG Hammitt, C Chao, CL Kling, TM Mitchell, and DO Rogers. Astm round-robin test with vibratory cavitation and liquid impact facilities of 6061-t 6511 aluminum alloy, 316 stainless steel and commercially pure nickel. *Mater Res Stand*, 10(10):16–23, 1970.

[70] PA March. Evaluating the relative resistance of materials to cavitation erosion: a comparison of cavitating jet results and vibratory results. In *ASME cavitation and multiphase flow forum, Cincinnati*, pages 14–17, 1987.

[71] M K Lee, W W Kim, C K Rhee, and W J Lee. Liquid impact erosion mechanism and theoretical impact stress analysis in tin-coated steam turbine blade materials. *Metallurgical and Materials Transactions A*, 30(4):961–968, 1999.

[72] W Pfitsch, S Gowing, D Fry, M Donnelly, and S Jessup. Development of measurement techniques for studying propeller erosion damage in severe wake fields. In *7th international symposium on cavitation (CAV2009), Ann Arbor, Michigan*, pages 17–22, 2009.

[73] A Philipp and W Lauterborn. Cavitation erosion by single laser-produced bubbles. *Journal of Fluid Mechanics*, 361:75–116, 1998.

[74] M Dular, O C Delgosha, and M Petkovšek. Observations of cavitation erosion pit formation. *Ultrasonics sonochemistry*, 20(4):1113–1120, 2013.

[75] G L Chahine, Franc J P, and Karimi A. Cavitation impulsive pressures. In K-H Kim, G L Chahine, J-P Franc, and A Karimi, editors, *Advanced Experimental and Numerical Techniques for Cavitation Erosion Prediction*, pages 71–95. Springer, 2014.

[76] GL Chahine, R Annassami, CT Hsiao, and GS Harris. Scaling rules for the prediction on undex bubble re-entering jet parameters. *SAVIAC Critical Technologies in Shock and Vibration*, 4(1):1–12, 2006.

[77] A Norris. Eulerian conjugate stress and strain. *Journal of Mechanics of Materials and Structures*, 3(2):243–260, 2008.

[78] Ted Belytschko, Wing Kam Liu, Brian Moran, and Khalil Elkhodary. *Nonlinear finite elements for continua and structures*. John wiley & sons, 2013.

[79] H Xiao, OT Bruhns, and A Meyers. Hypo-elasticity model based upon the logarithmic stress rate. *Journal of Elasticity*, 47(1):51–68, 1997.

[80] H Xiao, OT Bruhns, and A Meyers. Direct relationship between the lagrangean logarithmic strain and the lagrangean stretching and the lagrangean kirchhoff stress. *Mechanics Research Communications*, 25(1):59–67, 1998.

[81] Heng Xiao, Otto Timme Bruhns, and Albert Thomas Marie Meyers. Strain rates and material spins. *Journal of Elasticity*, 52(1):1–41, 1998.

[82] Thomas JR Hughes and James Winget. Finite rotation effects in numerical integration of rate constitutive equations arising in large-deformation analysis. *International journal for numerical methods in engineering*, 15(12):1862–1867, 1980.

[83] Meyers A, Xiao H, and Bruhns OT. Elastic stress ratchetting and corotational stress rates. *Tech. Mech*, 23:92–102, 2003.

[84] V Agrawal, K Holzworth, W Nantasetphong, AV Amirkhizi, J Oswald, and S Nemat-Nasser. Prediction of viscoelastic properties with coarse-grained molecular dynamics and experimental validation for a benchmark polyurea system. *Journal of Polymer Science Part B: Polymer Physics*, 2016.

[85] Z Jia, AV Amirkhizi, W Nantasetphong, and S Nemat-Nasser. Experimentally-based relaxation modulus of polyurea and its composites. *Mechanics of Time-Dependent Materials*, pages 1–20, 2016.

[86] JD Ferry. *Viscoelastic properties of polymers*. John Wiley & Sons, 1980.

[87] J Zhao, WG Knauss, and G Ravichandran. Applicability of the time–temperature superposition principle in modeling dynamic response of a polyurea. *Mechanics of Time-Dependent Materials*, 11(3-4):289–308, 2007.

[88] WG Knauss. Viscoelastic material characterization relative to constitutive and failure response of an elastomer. Technical report, DTIC Document, 2004.

[89] Sarva SS, Deschanel S, Boyce MC, and Chen W. Stress–strain behavior of a polyurea and a polyurethane from low to high strain rates. *Polymer*, 48(8):2208–2213, 2007.

[90] M Grujicic, R Yavari, JS Snipes, S Ramaswami, T Jiao, and RJ Clifton. Experimental and computational study of the shearing resistance of polyurea at high pressures and high strain rates. *Journal of Materials Engineering and Performance*, 24(2):778–798, 2015.

[91] HJ Qi and MC Boyce. Constitutive model for stretch-induced softening of the stress–stretch behavior of elastomeric materials. *Journal of the Mechanics and Physics of Solids*, 52(10):2187–2205, 2004.

[92] JS Bergström and MC Boyce. Constitutive modeling of the large strain time-dependent behavior of elastomers. *Journal of the Mechanics and Physics of Solids*, 46(5):931–954, 1998.

[93] A Peterlin. Plastic deformation of crystalline polymers. *Polymer Engineering & Science*, 17(3):183–193, 1977.

[94] J Mohanraj, MJ Bonner, DC Barton, and IM Ward. Physical and mechanical characterization of oriented polyoxymethylene produced by die-drawing and hydrostatic extrusion. *Polymer*, 47(16):5897–5908, 2006.

[95] F Addiego, A Dahoun, C G'Sell, and JM Hiver. Characterization of volume strain at large deformation under uniaxial tension in high-density polyethylene. *Polymer*, 47(12):4387–4399, 2006.

[96] H Martin. Heat and mass transfer between impinging gas jets and solid surfaces. In *In: Advances in heat transfer. Volume 13. New York, Academic Press, Inc., 1977, p. 1-60.*, volume 13, pages 1–60, 1977.

[97] RJ Asaro, B Lattimer, C Mealy, and G Steele. Thermo-physical performance of a fire protective coating for naval ship structures. *Composites Part A: Applied Science and Manufacturing*, 40(1):11–18, 2009.

[98] MJ Assael, KD Antoniadis, and JT Wu. New measurements of the thermal conductivity of pmma, bk7, and pyrex 7740 up to 450k. *International Journal of Thermophysics*, 29(4):1257–1266, 2008.